Effect of boulder size on ejecta velocity scaling law for cratering and its implication for formation of tiny asteroids

Okawa, Hatsune ; Arakawa, Masahiko ; Yasui, Minami ; Hasegawa, Sunao ; Toda, Mizuno ; Shirai, Kei ; Yamamoto, Yuya

(Citation)
Icarus,387:115212

(Issue Date)
2022-11-15

(Resource Type)
journal article

(Version)
Accepted Manuscript

(URL)
https://hdl.handle.net/20.500.14094/0100476894

Effect of boulder size on ejecta velocity scaling law for cratering and its implication for formation of tiny asteroids

Hatsune Okawa[1], Masahiko Arakawa[1*], Minami Yasui[1], Sunao Hasegawa[2], Mizuno Toda[3], Kei Shirai[1], Yuya Yamamoto[1]

1. Graduate School of Science, Kobe University, 1-1, Rokkodai-cho, Nada-ku, Kobe 657-8501, Japan
2. Institute of Space and Astronautical Science, Japan Aerospace Exploration Agency, Sagamihara, 252-5210, Japan
3. Faculty of Science, Kobe University, 1-1, Rokkodai-cho, Nada-ku, Kobe 657-8501, Japan

*Author for Correspondence: Masahiko Arakawa, Graduate School of Science, Kobe University, 1-1, Rokkodai-cho, Nada-ku, Kobe 657-8501, Japan; Tel: +81-78-803-6684; Fax: +81-78-803-6684; E-mail: masahiko.arakawa@penguin.kobe-u.ac.jp

Manuscript pages: 35

Number of figures: 16

Number of tables: 2

Abstract

Ejecta velocity distribution is an important property for controlling asteroid surface evolution and for changing the size frequency distribution of asteroids and planetary dusts. Recent asteroid explorations revealed that boulders on an asteroid surface had a wide size frequency distribution. On the other hand, many studies on ejecta velocity distribution for cratering experiments used fine-grained homogeneous targets. Thus, to study the ejection process of various-sized boulders on rubble-pile asteroids, we conducted impact experiments using gas guns at impact velocities of 100 m s^{-1} to 4 km s^{-1} on targets with various-sized glass beads, and analyzed boulder trajectories in three dimensions to clarify the effect of grain size on ejection velocity distribution. The results showed that the ejection velocity, v_0, decreased as the bead size increased, and the ejecta velocity scaling law was improved to $\frac{v_0}{\sqrt{gR}} = k_2{}' \left(\frac{r_0+a}{R}\right)^{-\frac{1}{\mu'}}$ including the bead radius, a; r_0 is the initial position of the bead, g is the gravitational acceleration, R is the crater radius, and $k_2{}'$ and μ' are, respectively, 0.58 ± 0.02 and 0.62 ± 0.02 for the low-impact velocity range (<200 m s^{-1}) and 0.61 ± 0.07 and 0.57 ± 0.04 for the high-impact velocity range (>1 km s^{-1}). Using our improved ejecta velocity scaling law, we calculated the landing points of ejected boulders and concluded that boulders with radii > $0.34R$ could not be ejected outside the final crater. Moreover, when the Urashima crater on asteroid 162173 Ryugu was formed on the surface, boulders up to 64 m in diameter may have been ejected beyond the escape velocity of Ryugu to become tiny monolithic asteroids.

Key words:

Asteroids; Cratering; Impact processes; Regoliths

1. Introduction

1.1. Background

Impact crater formation is a major process that resurfaces asteroids and affects their surface evolution. During the crater growth process, subsurface materials are excavated and ejected from the impact crater. Ejected materials whose ejection velocities exceed the asteroid's escape velocity would escape from the parent body, thus creating the numbed of new small bodies and dusts, some of which could strike Earth as meteorites. On the other hand, ejected materials whose ejection velocities are smaller than the asteroid's escape velocity would deposit on the asteroid surface. Since the area deposited by the ejecta is generally larger than that excavated by the cratering process, the ejecta deposition process also affects the asteroid' surface evolution. Therefore, the velocity distribution of ejected materials would determine whether the ejecta is deposited on the asteroid surface or escape from the asteroid. The distribution is thus a very important factor in asteroid surface evolution and changes the size frequency distribution of asteroids and planetary dust.

To speculate on planetary-scale impact phenomena based on laboratory experiments, it is necessary to study the scaling laws for ejecta velocity distributions (Housen and Holsapple, 2011). Oberbeck and Morrison (1976) conducted impact experiments using fine-grained quartz sand as a target. They divided the ejecta curtain into blocks of different heights using ladder-like slits, and observed the trajectory of each cluster using a high-speed video camera to determine the ejection velocity. They found that the ejection velocity decreased as the distance from the impact point

63 increased. Cintala et al. (1999) observed the trajectory of individual ejecta particles by illuminating
64 the ejecta curtain with a sheet light source and taking flash photography. The ejecta velocity
65 distributions obtained in their experiments followed a power-law-type scaling law for ejecta
66 velocity based on the dimensional analysis by Housen et al. (1983). Hermalyn and Schultz (2011)
67 used quartz sand with a diameter of 1 mm as a target and recorded the crater formation process
68 using a high-speed video camera to analyze the ejection velocity by Particle Tracking Velocimetry
69 (PTV). Moreover, Tsujido et al. (2015) conducted impact experiments using quartz sand with a
70 diameter of 500 μm, recorded the ejecta curtain by a high-speed video camera, and tracked each
71 particle at the outer edge of the ejecta curtain on the images to determine the ejection velocity. In
72 these two studies, the scaling law for ejecta velocity distribution was obtained for various
73 projectiles with different densities and sizes. Thus, the ejection velocity distribution characterized
74 by the slope of power-law-type relationship between the initial position and the ejection velocity
75 was found to slightly depend on the projectile density: The slope became greater for low-density
76 projectiles.

77 Recent asteroid explorations observed that some asteroids, such as Itokawa, Ryugu, and Bennu,
78 were covered with various-sized boulders and that the surfaces included a lot of boulders ranging
79 from several meters up to decameters. Those surface boulders had a power-law-type size frequency
80 distribution in a wide range of boulder sizes, and respective power law indices of -3.1 and -2.7
81 were obtained for Itokawa (Michikami et al., 2008) and Ryugu (Michikami et al., 2019). However,

82 those experiments introducing in the previous paragraph used only fine-grained targets whose
83 single grains were smaller than 1 mm, which was less than the projectile size. How the size
84 frequency distribution of the target grains affected the scaling laws for the cratering process has
85 not been explained. Thus, it is necessary to elucidate these effects on the ejecta velocity scaling
86 law in order to study resurfacing and the process by which boulders escape rubble-pile bodies.
87 Several cratering experiments using coarse-grained targets have been conducted to investigate
88 the effect of grain size; actually, the size ratio of the target grain to the projectile is crucial. For
89 example, Güttler et al. (2012) conducted impact experiments on the armoring effect using glass
90 bead targets (0.2–30 mm in the diameter) and a glass sphere projectile (1–8 mm in the diameter).
91 They found that the crater diameter suddenly halved when the size ratio of the target grain to the
92 projectile changed from 1 to 10. Barnouin et al. (2019) also conducted impact experiments using a
93 1:1 size ratio of the target grain to the projectile and found asymmetries in the crater shape and the
94 ejection angle as well as large scattering in the ejection velocity at a given ejection position. The
95 asymmetries and scattering could be caused by the initial interactions between the projectile and
96 the target grain. Yasui et al. (2021) focused on the size distribution of the target grains and
97 conducted impact experiments using mixed targets with equal masses of glass beads 0.1, 1, 3, and
98 10 mm in diameter. They found that at low impact velocities, the crater size of the mixed target
99 was slightly smaller than that of the homogeneous target with a diameter of 0.1 mm. As described
100 above, few studies on ejecta velocity have focused on ejecta grain size, and the effect of grain size

101 on the scaling law of ejecta velocity distribution is still unclear.

102 In April 2019, an impact experiment was conducted on the asteroid Ryugu by a Small Carry-on
103 Impactor (SCI) aboard the spacecraft Hayabusa2 (Arakawa et al., 2020). Although the surface of
104 Ryugu was covered by regolith and boulders with a size frequency distribution up to 160 m
105 (Michikami et al., 2019) and the SCI-aimed region was filled with meter-sized boulders, the SCI
106 crater was found to have formed in the gravity-dominated regime and the crater size was the same
107 as that expected from the crater size scaling law for a dry-sand target: The armoring effect due to
108 the large boulders was not recognized. Therefore, it is expected that the excavation flow during
109 SCI crater formation is almost the same as that induced in a homogeneous fine-grained target. This
110 excavation flow ejected boulders up to 1 m in diameter out of the crater, and a boulder about 6 m
111 remained in the crater (Honda et al. 2021). Both the ejected boulders and the remaining one were
112 expected to move with the crater excavation flow. Thus, to simulate the elementary process of
113 boulder movement on Ryugu by the SCI impact in the laboratory, it is suitable to use a granular
114 target composed of single particle size called a homogeneous target on which various-sized
115 particles simulating boulders are set.

116 Therefore, in this study, we clarified the scaling law for the velocity distribution of boulders
117 ejected by excavation flow induced in a homogeneous target. In particular, we investigated the
118 effect of boulder size on ejecta velocity distribution. We also estimated the maximum boulder size
119 that could escape from the parent body by cratering based on the ejecta velocity distribution

120 considering the effect of boulder size.

121

122 **1.2. π-Scaling theory**

123 Ejecta velocity distribution was studied by using the π-scaling theory summarized by Housen
124 and Holsapple (2011). This theory allowed us to extrapolate our results to planetary-scale impacts.
125 In this section, we summarize the scaling law for ejecta velocity distribution in the crater formation
126 process.

127 Figure 1 schematically illustrates the ejection process during crater formation. The π-scaling Fig. 1
128 law is based on the assumption of a point source approximation, and it is also assumed that cratering
129 process does not depend on parameters related to projectile properties, r_p, v_i, and ρ_p individually,
130 but rather depend on the quantity of C, which is defined by the combination of these parameters,

131 $$C = r_p {v_i}^{\mu} {\rho_p}^{\nu}, \quad (1)$$

132 where r_p, v_i, and ρ_p are the impactor radius, impact velocity and impactor density,
133 respectively; ν and μ are constants obtained from laboratory experiments. C is a coupling
134 parameter. Introducing this coupling parameter, C, the ejecta velocity, v_0, can be described as
135 follows according to the π-scaling law,

136 $$\frac{v_0}{v_i} = k_1 \left[\frac{r_0}{r_p} \left(\frac{\rho_t}{\rho_p} \right)^{\nu} \right]^{-1/\mu}, \quad (2)$$

137 where ρ_t and r_0 are the target density and initial position of an ejecta particle, respectively; k_1
138 is a constant obtained from laboratory experiments. In addition, the crater radius R in the gravity-

dominated regime is expressed as follows in the π-scaling law,

$$R\left(\frac{\rho_t}{m}\right)^{1/3} = H_1\left(\frac{\rho_t}{\rho_p}\right)^{(2+\mu-6\nu)/[3(2+\mu)]}\left[\frac{g r_p}{{v_i}^2}\right]^{-\mu/(2+\mu)}, \quad (3)$$

where g and H_1 are gravitational acceleration and a constant obtained from laboratory experiments, respectively. From the above equations, the scaling law for the ejecta velocity distribution in the gravity-dominated regime can be written as,

$$\frac{v_0}{\sqrt{gR}} = k_2\left(\frac{r_0}{R}\right)^{-1/\mu}, \quad (4)$$
$$k_2 = k_1\left((4\pi/3)^{1/3}H_1\right)^{-(2+\mu)/2\mu}.$$

Impact cratering experiments using homogeneous sand targets have confirmed that the ejecta velocity distribution can be well approximated by Eq. (4), (e.g., Tsujido et al., 2015). However, Eq. (4) does not include the effects of ejecta particle sizes, especially for particles large enough compared to the crater radius. Moreover, the effects of the size distribution of ejecta particles are not included either, although both effects would be important on the real asteroid surface. We now are not sure whether the ejecta scaling law is still valid for targets with ejecta particles whose sizes cannot be ignored or for targets composed of ejecta particles with a size distribution. Therefore, here we studied the effects of particle sizes on the ejection velocity distribution.

2. Experimental methods

2.1. Impact experiments

We conducted impact cratering experiments by using a one-stage vertical gas gun at Kobe

157 University and a two-stage vertical gas gun at ISAS/JAXA. Both apparatuses have a large vacuum
158 chamber with large transparent windows on the sides in which the target is set, enabling us to
159 observe the crater formation process.

160 The two apparatuses have different impact velocity ranges. We performed relatively low-
161 velocity impact experiments ranging from 101 to 191 m s^{-1} at Kobe University and relatively high-
162 velocity impact experiments ranging from 1.93 to 4.42 km s^{-1} at ISAS. At Kobe University, we
163 used a spherical projectile made of stainless steel (SUS) with a diameter of 3 mm. The densest
164 impactors in asteroids could be iron meteorite parent bodies and/or orbiting boulders with the
165 density like iron meteorite. By using this type of projectile, we can study the upper limit of the
166 density effect on the cratering processes. The vacuum chamber was evacuated below 10^3 Pa before
167 the shot. At ISAS, we used spherical projectiles made of SUS with diameters of 1 mm and 2 mm.
168 The vacuum chamber was evacuated below 4 Pa before the shot.

169 We used glass beads with a median diameter of about 100 μm as a target. The angle of repose
170 and the bulk density of the glass beads were 23 ± 1° and 1.42 g cm^{-3}, respectively; the estimated
171 porosity was 43% due to the grain density of each glass bead, 2.5 g cm^{-3}. A container 28 cm in
172 diameter and 10 cm in depth was used to prepare the target, and it was filled with the glass beads.
173 To prepare a smooth surface that matched the height of the container, the target surface was
174 flattened by using a metal plate.

175 To study the effects of particle sizes on the ejecta velocity distribution, we used colored beads

of various sizes (Fig. 2). We used five types of colored beads, which we call tracer beads, with diameters of 3, 5, 10, 17, and 30 mm. We chose these diameters because the minimum of 3 mm is enough larger than 0.1 mm of target fine glass beads and the maximum of 30 mm is slightly smaller than the crater rim radius in this study. They were large enough to be tracked in high-speed images, and the differences in their sizes were large enough to investigate the dependence of velocity distribution on size. All tracer beads numbered 1–50 were placed on the target surface except for the impact point, which was just below the gun muzzle. We placed the tracer beads within the final crater area closer to the high-speed cameras because they were hidden by the ejecta curtain and not visible when placed on the far side of the impact site from the cameras. The tracer beads were placed in a grid or randomly, with the distance between them at least as large as the particle radius, so that they did not collide with each other during ejection. To determine the initial positions of the tracer beads accurately, we buried them to half of their volume, so that we could measure their positions accurately by the camera images before the shot. Due to the limited number of colors available, it was not possible to paint each bead with a different color, so we placed tracer beads with different colors next to each other as much as we could. The combination of tracer bead sizes depended on the experiments as shown in Table 1.

Fig. 2

Additionally, we also studied the effect of buried depth of a tracer bead on the ejection velocity. In our standard tests, a hemisphere of tracer bead was buried in fine glass beads target. In order to study the effect of buried depth of a tracer bead, several additional experiments were conducted for

a tracer bead put on the target surface without burial depth and for a tracer bead completely buried in the target. Large tracer beads with the diameter of 10 and 17 mm were used to control the depth accurately.

After the target preparation, the target container was set in a vacuum chamber, which was evacuated before the shot.

2.2. Observation

One of the purposes of this study was to three-dimensionally track ejecta particles, so it was necessary to observe and track the same particle using two cameras. We used two synchronized high-speed cameras triggered by a velocity meter. These cameras enabled us to obtain the three-dimensional trajectories of the tracer beads. The cameras were positioned appropriately to observe the entire target surface and the movement of all tracer beads (Fig.3). The line of sight of one camera crossed that of the other at angles from 45º – 90º, and the plane including these two lines of sight had an angle against the target surface from 30º – 90º. The parallax caused by these angles was large enough to analyze the high-speed images in order to obtain three-dimensional trajectories. High-speed images were taken at 2000 – 10000 frames per second; the image fields were 1024 × 768 and 1920 × 1080 pixels, so that the image resolution was from 0.18 – 0.28 mm/pixel. The exposure time was set at 20 – 330.7 μs. In each experiment, the target surface was illuminated by bright LED lights to identify the tracer beads. Since the tracer beads were colored brightly, it was

Fig. 3

easy to trace their trajectories during the crater formation process. The colors helped us to identify and track the same particles by the two cameras to obtain a three-dimensional view.

The crater rim diameter, D_{rim}, was measured by using a digital caliper and by analyzing photos taken from the top of the impact crater. We measured it in four directions and used the average as D_{rim}. The crater size scaling laws are conventionally constructed for crater radius, *R*, but not for rim radius, R_{rim}, in Fig.1. So, we estimated the crater radius, R, from the crater rim radius, $R_{\mathrm{rim}} = D_{\mathrm{rim}}/2$, by using the previous measurements for similar fine glass beads target of $R = R_{\mathrm{rim}}/1.23$ (Yasui et al., 2021). Moreover, it is well known that the transient crater slightly deforms to be the final crater and widens in the diameter for fine glass beads target. The ratio of the final crater diameter to the transient crater diameter for glass bead targets has been studied by Yamamoto et al. (2006) and it was obtained to be 1.05 for the target composed of 72 μm sized glass beads target.

2.3. Analytical methods

2.3.1. Determination of tracer trajectory in three dimensions

To obtain the position of a tracer bead in a three-dimensional coordinate system, it is necessary to define the coordinate system in the target chamber. In this study, we used as reference an acrylic box of 40 × 30 × 30 cm with grid lines to determine the three-dimensional scale. The grid interval was prepared from 2 to 5 cm according to the size of the area to be recorded by the cameras. The

reference box was placed in the target chamber before the shot and removed after the calibration; the box was recorded as still images by the two high-speed cameras. The reference images allowed us to define the origin as one of the corners of the box, and then we defined the three-dimensional coordinate system: The xy axes were defined on the bottom of the reference box and the z was defined as the axis perpendicular to the xy plane. When the camera positions were shifted accidentally, the reference box was recorded again for recalibration.

The three-dimensional(3D) trajectory of the tracer bead is determined by means of stereo vision. First, we obtained the position of the tracer bead in two-dimensional (2D) pixel coordinates from the images recorded by the cameras (Fig. 3a, b). Then, we converted these 2D pixel coordinates of the tracer bead into the 3D coordinates defined above (Fig. 3c). The camera projection matrix necessary for this conversion was determined from pairs of intersection points of grid lines of the reference box mentioned above. By using the method, we could determine the location of a tracer bead within 0.3 mm as typical error.

Next, to determine the trajectory of the tracer bead, we selected 7–30 images during the ejection process in which the tracer bead could be clearly observed by both cameras, then analyzed the 3D coordinates on each image. The initial position of the tracer bead in the 3D coordinate system was measured from the image before the shot by using same method. In each experiment, we placed 10–50 tracer beads on the target surface, but it was impossible to analyze the trajectories of all tracer beads because many of them were hidden by the ejecta curtain. Therefore, we analyzed the

252 3D coordinates of 1–7 tracer beads whose trajectories could be observed by both cameras in each

253 experiment.

254

255 **2.3.2. Determination of ejection position, velocity, and angle**

256 Figure 4 shows the ejection vector of a tracer bead and parameters. To obtain the ejecta velocity Fig. 4

257 distribution, it is necessary to determine the initial position r_0 and the ejection velocity v_0 for

258 each tracer bead. We defined the initial position r_0 as the distance between the impact point of the

259 projectile, $(x_\mathrm{i}, y_\mathrm{i}, z_\mathrm{i})$, and the ejection position of the tracer bead, (x_0, y_0, z_0), which was analyzed

260 by the method described in section of 2.3.1.

261 The ejection velocity of a tracer bead, v_0, is determined from the relationship between the

262 measured displacement and time. Therefore, we analyzed the trajectories of the tracer beads after

263 the impact in the xyz coordinate system and determined the xyz components of the ejection

264 velocity, v_x, v_y, and v_z. The v_0 is determined by the following equation:

265 $$v_0 = \sqrt{{v_x}^2 + {v_y}^2 + {v_z}^2}\,. \tag{10}$$

266 By using each component of the ejection velocity obtained by the above method, the ejection angle,

267 θ, is determined according to the following equation:

268 $$\theta = \tan^{-1}\frac{v_z}{\sqrt{v_x^2 + v_y^2}}\,. \tag{11}$$

269 The azimuthal angle, ϕ, between the ejection vector projected on the xy plane and the x axis

270 defined in Fig. 4 is calculated by using an impact point, an ejection point, and ejection velocity as

follows:

$$\phi = \left| \tan^{-1} \frac{y_\mathrm{i} - y_0}{x_\mathrm{i} - x_0} - \tan^{-1} \frac{v_y}{v_x} \right| . \quad (12)$$

3. Results

3.1. Observations of crater formation

Figure 5 shows a series of images of the crater formation in run number 210317-8. At 1 ms after impact, the ejecta curtain has an inverted cone shape near the impact point. As time passes, the growth of the ejecta curtain is partly prevented by the tracer beads. At 3 ms, the ejecta curtain reaches 3 tracer beads positioned near the impact point and becomes separated by the tracer beads, and hole-like open spaces above them are formed. At 10–70 ms, the tracer beads are lifted off and ejected from the target surface after the ejecta curtain passes. The open spaces above the tracer beads grow larger and larger, and thus a ray structure develops in the ejecta curtain. At 110 ms, the crater growth has already stopped and the ejecta curtain begins to deposit on the surface while it keeps the ray structure. The ejected tracer beads start to fall or deposit on the target surface. At 180 ms, the ejecta curtain goes outside of the container and all ejected tracer beads deposit on the target surface. The crater left on the surface has a cone shape with deposition rim, and it was found that the crater rim radius did not change regardless of the presence or absence of the tracer beads (Yasui et al., 2021).

Fig. 5

3.2. Scaling of ejecta velocity distribution

All the experimental data for the ejection velocities of tracer beads are summarized in Table 2. In order to avoid a projectile direct collision onto a tracer bead, a tracer bead was put at r_0 larger than a, so that the data with large a/R distributed near the crater rim and the data with smaller a/R distributed even at smaller r_0 in Fig. 6. While we could not measure the ejection velocities of tracer beads put near the impact point < 0.18 because the beads were hidden in the ejecta curtain at the observable area by high-speed cameras. Figure 6a shows the ejecta velocity distribution of tracer beads obtained in the low-velocity experiments, and it indicates the relationship between the initial position normalized by the crater radius, r_0/R, and the ejection velocity, v_0, normalized by $\sqrt{gR}$. The symbol color shows the ratio of the radius of the tracer bead to the crater, a/R. Although the ejection velocity decreased exponentially with the increase in the normalized initial position following Eq. (4), the ejection velocity decreased systematically when the bead size increased. This means that the ejecta velocity distribution would depend on the beads size.

Fig. 6

The initial position r_0 is the distance from the impact point to the center of the bead (Fig. 1), but it is unclear whether r_0 is a suitable distance for the scaling of ejecta velocity distribution or not, since the diameter of the tracer beads is too large to approximate it at a mass point and is at least 30 times that of the surrounding target beads (100 μm). Hence, we replotted Fig. 6a regarding the initial position of the tracer beads: The size range of the tracer beads was introduced for each velocity datum in Fig. 6b and 6c; the size range is described by outer and inner edges, which are

309 defined as $r_0 + a$ and $r_0 - a$, respectively (Fig.1). Then, we clearly notice that the outer edge of
310 the tracer beads has a very good correlation between ejection velocity and initial position
311 irrespective of bead size, although the inner edge looks scattered. But it is unclear why the outer
312 edge of a tracer beads is suitable for the initial position to scale the tracer beads with different sizes,
313 so this physical mechanism should be studied quantitatively by using numerical simulations in the
314 future. Qualitative considerations for the following improved scaling relationship are given in the
315 discussion section.

316 Therefore, we recalculated the relationship by using the initial position, $r_0 + a$, which means
317 the distance from the impact point to the outer edge of the bead, instead of r_0 (Fig. 6c). As a result,
318 the normalized ejection velocity was well scaled by $r_0 + a$, and it did not depend on the bead size
319 anymore. This improved relationship is written by the Eq. (4) with $r_0 + a$ instead of r_0,

320 $$\frac{v_0}{\sqrt{gR}} = k_2{}' \left(\frac{r_0 + a}{R}\right)^{-\frac{1}{\mu'}}. \quad (13)$$

321 We determined the constants $k_2{}'$ and μ' by using the least-square method to be 0.58±0.02 and
322 0.62±0.02, respectively. The results for the high-velocity impact experiments are also plotted on Fig. 7
323 Fig. 6d, e, f and we also recognize that $r_0 + a$ can scale the ejection velocity well.

324 Figure 7 shows the velocity distributions of tracer beads obtained for the low- and high-velocity
325 impact experiments. The ejection velocities of the high-velocity experiments are also well
326 described by Eq. (13); that is, the size of a tracer bead is scaled by $r_0 + a$, though the high-velocity
327 data are slightly scattered compared with the low-velocity data. The slope of the velocity

distribution differs between them; the slope is steeper for the high-velocity impact. We determined the constants k_2' and μ' by using the least-square method to be 0.61 ± 0.07 and 0.57 ± 0.04, respectively, and μ' for the high-velocity impact was 0.05 less than that for the low-velocity impact: μ' could depend on the impact velocity. But, k_2' would be the same value in both velocity ranges within the errors.

Tsujido et al. (2015) found that μ depended strongly on the projectile materials and that the penetration depth could, depending on the projectile material, cause the difference in μ. Thus, we speculate that the penetration depth could depend on the impact velocity causing the difference in μ'. Cintala et al. (1999) and Anderson et al. (2007) measured ejecta velocity distributions for sand targets and obtained μ values from the slope of the distribution; they are 0.58 ($\pm$0.05) for Cintala et al. using Al projectile with the velocity from 0.8 to 1.9 kms^{-1} and 0.58 ($\pm$0.11) for Anderson et al. using glass bead projectile with the velocity from 0.3 to 1.7 kms^{-1}. Unlike our results, they did not find clear velocity dependence on μ in their velocity range below 2 kms^{-1}, which may be due to errors. Although the density of their projectiles is 2.5~2.7 gcm^{-3} and rather smaller than that of our SUS projectile of 7.8 gcm^{-3}, the μ' for our high-velocity impacts is almost consistent with those of their studies. This may mean that the density dependence on μ found in low velocity (Tsujido et al., 2015) is weakened or disappeared in high-velocity range >~2 kms^{-1}. Therefore, our μ' could be applicable to other projectiles with the density like rocky materials.

3.3. Ejecta curtain pattern

Figure 8a shows a snapshot of the ejecta curtain taken by the high-speed camera at 10 ms after the impact (Run 210318-1). You can see several oval holes appearing on the curtain, and the oval holes look grey compared to their surroundings. We notice that the tracer beads are fixed to the bottom each hole. The area surrounded by a dotted rectangle on the curtain image is magnified and displayed on the right, showing that the tracer beads are placed at the bottom of the oval hole in this image. This oval hole should be a forbidden zone formed by a tracer bead: The ejecta flow was stopped by a tracer bead positioned at r_0 with the radius of a so that the fine glass beads did not eject into the grey zone in Fig. 8b. Fig. 8b shows a schematic illustration of the ejecta curtain at the timing described in Fig. 8a. The forbidden zone caused by the tracer bead is shown by a grey color, and the ejecta curtain shape is shown in the cross section together with the tracer beads at the initial position and the speculated moved positions A, B, C with the ejection velocity of $v_0(r_0\text{-}a)$, $v_0(r_0)$, and $v_0(r_0+a)$, respectively. The front view of the ejecta curtain with an oval hole caused by a tracer bead is shown at the left. The tracer bead is positioned at A, B, and C in the forbidden zone according to each ejection velocity. If the tracer bead has the ejection velocity, v_0, ejected from r_0-a, the bead is positioned at A, and it appears at the top of the oval hole. Similarly, if the tracer bead velocity is $v_0(r_0)$, the bead is positioned at B, and it appears at the center of the oval hole. In fact, the tracer bead appeared at the bottom of the hole, so the ejection velocity of the tracer bead should be $v_0(r_0+a)$ and it strongly supports our improved scaling law.

Fig. 8

366

367 **3.4. Ejection angle, azimuthal angle**

368 Figure 9a shows the relationship between the initial position normalized by the crater radius, Fig. 9

369 r_0/R, and the ejection angle, θ, of each tracer bead; these data include the results of both high-

370 and low-impact velocity experiments. The ejection angle is within 50-60º in the r_0/R range of

371 $0.1-0.4$. As the r_0/R is larger than 0.4, the θ decreases gradually to 30º, although the θ

372 depends slightly on the a/R. Tsujido et al. (2015) found that the maximum of the ejection angle

373 at each initial position decreased with increasing distance from the impact point from 50º to 30º.

374 Our decreasing trend of the ejection angle at the initial position $> 0.4R$ is similar to their results,

375 though the θ around $r_0/R = 0.4$ is about 55º, which is larger than that of Tsujido et al. (2015)

376 due to the difference in the target material.

377 The ejection angle of a larger tracer bead looks smaller and the θ could be changed with a/R

378 systematically. Therefore, as with the scaling of the velocity distribution, we replotted the ejection

379 angle with $(r_0 + a)/R$ as the horizontal axis. As a result, the ejection angles for various a/R are

380 well scaled in this figure, as shown in Fig. 8b. The ejection angles can be fitted by the equation,

381 $$\theta = -15.3\left(\frac{r_0 + a}{R}\right) + 60.4. \quad (14)$$

382 This scaling does not depend on the impact velocity, unlike the case with ejecta velocity distribution.

383 A few points at $(r_0 + a)/R$ around 1 appear to drop from Eq. (14). This might be due to the effect

384 of the crater edge: Part of the large tracer beads was set outside the crater radius at the initial

position, so that part was not pushed by the excavation flow, and then the ejection angle of the tracer bead might shift to become smaller than the angle of the excavation flow.

Figure 10 shows the relationship between the initial position normalized by the crater radius, r_0/R, and the azimuthal angle, ϕ, of each tracer bead. All ϕ are very small, within 0º–10º, regardless of the initial position, and the ϕ did not depend on the a/R systematically. Therefore, the tracer beads eject radially from the impact point. Fig. 10

3.5. Rotation speed and effect of burial depth on ejection velocity

We made additional experiments to study the rotation speed of a tracer bead with a radius of 5 mm. Figure 11 shows the snapshots taken by the high-speed camera for the crater formation process made at the impact velocity of 152 ms^{-1}. A tracer bead ejected from the crater is successively recorded; the time after the impact of the projectile on the target surface is shown on each panel. We recognize that the ejecta curtain is split by the tracer bead and the tracer moves with the eject curtain embedded to the lower part of the bead. The tracer bead is painted in a striped pattern with white color, so we could measure the duration necessary for a half rotation. In this shot, the rotation speed is about 19 rad s^{-1} and the ejection velocity estimated from Eq. (13) is 1.27 ms^{-1}, so the rotational kinetic energy and the translational kinetic energy are calculated to be 3.3×10^{-6} J and 1.27×10^{-3} J, respectively. The energy partitioned into the rotational one is only 0.3 % of the total kinetic energy including the translational one. We also notice that the rotational direction of the Fig. 11

tracer bead is in the reverse direction, so called backspin. This rotational direction could be a hint to consider the reason why the tracer bead ejects at the velocity described in Eq. (13).

Figure 12 shows the ejecta velocity distribution obtained for the tracer beads not buried and completely buried in the target surface. It is noted that the ejection velocity for tracer beads set on the target surface called on-target bead is systematically smaller than that calculated from Eq. (13) for tracer beads buried a half of them even though the initial position is scaled by r_0+a/R. The ejection velocity of on-target bead is reduced to about 70 % of that calculated from Eq. (13) at each initial position. While the ejection velocity for a tracer bead buried completely called buried bead is slightly larger or almost on the line of Eq. (13) though there is only one data point. These results clearly show that the buried depth affects the ejection velocity when the buried depth is shallower than a half of the tracer bead, and the ejection velocity may not change at the buried depth deeper than a half of the bead.

4. Discussions

4.1. Effect of the crater edge

In the ejection angle distribution obtained in this study, we found the size effects of tracer beads: The ejection angles of large tracer beads departed from the linear function and decreased (Fig. 9b). Housen and Holsapple (2011) discussed that the ejection velocities of particles ejected from the region near the crater edge departed from the power-law dependence. They modeled this behavior

423 by assuming that the ejection velocity goes to zero at distance $r_0 = 1.23R$ and adding

424 $(1 - r_0/1.23R)^p$ to Eq. (2) for granular matters:

425 $$\frac{v_0}{v_i} = k_1 \left[\frac{r_0}{r_p}\left(\frac{\rho_t}{\rho_p}\right)^{\nu}\right]^{-\frac{1}{\mu}} \left(1 - \frac{r_0}{1.23R}\right)^{p}. \quad (15)$$

426 In this study, we used this model to modify the ejection velocity and angle distributions near the

427 crater edge (Fig. 13). The modified equations of ejection velocity distribution for low- and high- Fig. 13

428 impact velocity and the ejection angle distribution are described as follows:

429 $$\frac{v_0}{\sqrt{gR}} = k_2' \left(\frac{r_0 + a}{R}\right)^{-\frac{1}{\mu'}} \left(1 - \frac{r_0 + a}{1.23R}\right)^{0.1}, \quad (16)$$

430 $$\theta = \left(-6.4\frac{r_0 + a}{R} + 58.7\right)\left(1 - \frac{r_0 + a}{1.23R}\right)^{0.1}. \quad (17)$$

431 We chose the power law index of *p* to be 0.1 for the ejecta velocity distribution of both high- and

432 low-impact velocity, and this *p* of 0.1 can extrapolate these data toward the rim appropriately (Fig.

433 13a). The same *p* was used for Eq. (17) to fit the data in Fig. 13b though *p*=0.3 was adopted for

434 granular matter in Housen and Holsapple (2011).

435

436 **4.2. Effect of rotation on the ejection velocity**

437 The rotational kinetic energy was about 0.3 % of the total kinetic energy including the

438 translational kinetic energy, and the rotational direction of the tracer bead was observed to be

439 reverse direction (Fig. 11). Based on this evidence, we speculated that the tracer bead was mainly

440 accelerated by fine glass beads flowing closed to the outer edge of the tracer bead (see Fig. 14) Fig. 14

because the backspin of the tracer bead may occur by the upward torque exerted on the outer edge of the tracer bead (Fig. 1; Fig.14). Moreover, the fine glass beads flow close to the inner edge might escape upward from the surface without pushing the tracer bead, so that the fine glass beads flow of inner edge could not contribute the acceleration of the tracer bead enough. This may be the reason why the tracer bead has a velocity slower than that of the surroundings at r_0. But unfortunately, it is difficult for us to explain the quantitative mechanism of the scaled distance described as r_0+a in the improved scaling law. The geometrical relationship between the tracer bead and target fine glass beads should be important as is noticed for the burial depth effect on the ejection velocity. The momentum coupling between the tracer bead and the target fine glass beads was weaker for on-target bead, which is similarly to that occur at the inner edge of the tracer bead: A part of momentum of the fine glass beads flowing toward the tracer bead escapes from the target surface and the ejection velocity is reduced. However, the detail study to clarify the scaling of $(r_0+a)/R$ for tracer bead with the radius a is the future work, and we will study it using numerical simulations.

4.3. Boulder movement from the inside the crater

In this section, we discuss boulder movement from inside the crater during the crater formation process on rubble-pile asteroids. Boulders with initial ejection velocities higher than the escape velocity would escape from the asteroid and release into space to become a new tiny asteroid, while

boulders whose initial ejection velocities lower than escape velocity would land on the surface. Moreover, according to Eq. (16), we expect that a large boulder inside the crater could not move outside the crater, depending on its initial position. For example, an Iijima boulder on asteroid Ryugu with a diameter of 6 m moved only 2.6 m from its initial position, which was inside the SCI crater with a diameter of 14.5 m (Honda et al., 2021). Then, we calculated the landing points of boulders of various sizes ejected from inside the crater, and we also calculated the maximum size of a boulder that could escape from Ryugu during crater formation.

The landing point of a boulder with a ballistic trajectory can be calculated given the ejection velocity, v_0, and the ejection angle, θ. We define L as the distance between the impact point and the inner edge of the landed boulder (Fig. 1), and L is written as,

$$L = r_0 + \frac{{v_0}^2 \sin^2 2\theta}{g} - a, \tag{18}$$

and Eq. (16) is substituted in Eq. (18);

$$L = r_0 + R\left[k_2{}'\left(\frac{r_0 + a}{R}\right)^{-\frac{1}{\mu'}}\left(1 - \frac{r_0 + a}{1.23R}\right)^{0.1}\sin 2\theta\right]^2 - a, \tag{19}$$

where we notice that L is independent of the surface gravity, g.

Fig. 15

Figure 15 shows the contour plot of the landing point L normalized by the crater radius R, which is calculated by using Eq. (19) with the constants $k_2{}'$ and μ' for the high-impact velocity. The data at the initial position $r_0/R < a/R$ are not meaningful because the projectile collides with a boulder with radius a. Thus, we excluded the area above the line shown by $a/R = r_0/R$. Moreover, when part of the boulder is beyond the crater rim at the initial position $a/R > -r_0/R +$

479 1.23, the boulder might not move. Thus, we also excluded the area above the line shown by $a/R = 1.23 - r_0/R$. We then found that the boulder with $a/R > 0.615$ is never ejected from the crater. We can predict the normalized landing position, L/R, using the contours of Fig. 15. For example, it is recognized that a boulder with $a/R = 0.15$ can be ejected out of the crater rim with the initial position $r_0/R < 0.62$, and a boulder with $a/R = 0.3$ ejected from $r_0/R = 0.62$ lands on the inside of the crater at the landing position $L/R = 0.7$. As the crater rim corresponds to $L/R = 1.23$, we expect the boulder to land on the area out of the crater rim at $L/R = 1.23$. Thus, this contour shows that the maximum boulder size that can be ejected beyond the crater rim is $a/R = 0.34$: The maximum boulder size is simply proportional to the crater radius.

Applying Fig. 15 to the SCI crater with a diameter of 14.5 m, the maximum diameter of a boulder that can be ejected fully out of the crater from a position 2.5 m from the crater center is 5 m. The largest boulder ejected outside of the SCI crater was observed to be ~1.7 m (Honda et al., 2021). Moreover, an Iijima boulder with a size of 6 m was not ejected from the SCI crater, but moved 2.6 m inside the crater, and the moving distance calculated from this model is ~3 m, which is in good agreement with the observational result.

Fig. 16

Finally, we discuss the size of a boulder that could have escaped from Ryugu's gravitational field during the formation of the SCI and Urashima craters. Figure 16 shows the ejecta velocity distribution for grains with a size of $a/R = 0.04-0.40$. The horizontal lines represent the normalized escape velocity for Ryugu corresponding to the radii of the SCI and Urashima craters.

A dotted line is the normalized ejection velocity for the SCI crater corresponding to the escape velocity of Ryugu, $v_{\rm esc}/\sqrt{gR_{\rm SCI}}$. Ryugu's escape velocity is 0.37 m s^{-1}, its gravitational acceleration is 0.15 mm s^{-1} (Watanabe et al., 2019), and the SCI crater radius is 7.25 m. Therefore, the normalized escape velocity can be calculated as $v_{\rm esc}/\sqrt{gR_{\rm SCI}} = 11$. A dash-dotted line is the normalized ejection velocity for the Urashima crater corresponding to the escape velocity of Ryugu, $v_{\rm esc}/\sqrt{gR_{\rm Urashima}}$, and it is calculated to be 2.5 for the 145 m radius of the Urashima crater. When the normalized boulder radius, a/R, is larger than the normalized initial position, r_0/R, the projectile collides with the boulder directly, so we omit these ejecta velocities from this figure. In the case of the SCI crater, boulders could escape from Ryugu's gravity field when the normalized ejection velocity is greater than 11 and the initial position necessary for escaping is very close to the impact point: $r_0/R \leq 0.10$ for $a/R = 0.09$ and $r_0/R \leq 0.15$ for $a/R = 0.04$. Moreover, the boulders inside the SCI crater with $a/R > 0.09$, where $a > 0.65$ m, never escape from Ryugu. On the other hand, in the case of the Urashima crater with a diameter of 290 m (Hirata et al., 2020), boulders less than 64 m could escape from Ryugu to become new asteroids. The formation of a large crater such as Urashima is one of the mechanisms of generating new tiny monolithic asteroids, with sizes of dozens of meters, from boulders on rubble-pile asteroids.

Acknowledgements

We appreciate the assistance of Mr. Y. Yokota of Kobe University in the performance of these experiments. We also thank Dr. M. Kiuchi and Dr. Y. Shimaki of the Institute of Space and Astronautical Science for their help with the experiments. We would like to thank nac Image Technology Inc. for their technical assistance and high-speed camera rental. Our series of experiments were supported in part by the Hypervelocity Impact Facility at ISAS/JAXA. This work was supported in part by a Grant-in-Aid for Scientific Research (no. 16K17794 to M. Yasui and no. 16H04041 and no. 17H06459 to M. Arakawa) from the Japan Society for the Promotion of Science (JSPS).

References

Anderson, J. L. B., Cintala, M. J., Siebenaler, S. A., Barnouin-Jha, O. S. 2007. Ejecta-and size-scaling considerations from impacts of glass projectiles into sand. In Lunar and Planetary Science Conference, #2266.

Arakawa, M., Saiki, T., Wada, K., Ogawa, K., Kadono, T., Shirai, K., et al., 2020. An artificial impact on the asteroid (162173) Ryugu formed a crater in the gravity-dominated regime. Science 368, 67–71.

Barnouin, O.S., Daly, R.T., Cintala, M.J., Crawford, D.A., 2019. Impacts into coarse-grained spheres at moderate impact velocities: implications for cratering on asteroids and planets. Icarus 325, 67–83.

536 Cintala, M.J., Berthoud, L., Hörz, F., 1999. Ejection-velocity distributions from impacts into
537 coarse-grained sand. Meteorit. Planet. Sci. 34, 605–623.
538 Güttler, C., Hirata, N., Nakamura, A.M., 2012. Cratering experiments on the self armoring of
539 coarse-grained granular targets. Icarus 220, 1040–1049.
540 Hermalyn, B., Schultz, P.H., 2011. Time-resolved studies of hypervelocity vertical impacts into
541 porous particulate targets: Effects of projectile density on early-time coupling and crater
542 growth. Icarus 216, 269–279.
543 Hirata, N., Morota, T., Cho, Y., Kanamaru, M., Watanabe, S., Sugita, S., et al., 2020. The spatial
544 distribution of craters on Ryugu. Icarus 338, 113527.
545 Honda, R., Arakawa, M., Shimaki, Y., Shirai, K., Yokota, Y., Kadono, T., et al., 2021, Resurfacing
546 processes on asteroid (162173) Ryugu caused by an artificial impact of Hayabusa2's Small
547 Carry-on Impactor. Icarus 366, 114530.
548 Housen, K.R., Holsapple, K.A., 2011. Ejecta from impact craters. Icarus 211, 856–875.
549 Housen, K.R., Schmidt, R.M., Holsapple, K.A., 1983. Crater ejecta scaling laws: Fundamental
550 forms based on dimensional analysis. J. Geophys. Res. 88, 2485–2499.
551 Kadono, T., Suzuki, A. I., Matsumura, R., Naka, J., Suetsugu, R., Kurosawa, K., et al., 2020. Impact
552 experiment on asteroid (162173) Ryugu: Structure beneath the impact point revealed by in
553 situ observations of the ejecta curtain. Astrophys. J. Lett., 899 (1) (2020), p. L22.
554 Michikami, T., Honda, C., Miyamoto, H., Hirabayashi, M., Hagermann, A., Irie, T., et al., 2019.

555 Boulder size and shape distributions on asteroid Ryugu. Icarus 331, 179–191.
556 Michikami, T., Nakamura, A., Hirata, N., 2008. Size–frequency statistics of boulders on global
557 surface of Asteroid 25143 Itokawa. Earth Planets Space 56, 448–472.
558 Oberbeck, V.R., Morrison, R.H., 1976. Candidate areas for in situ ancient lunar materials. Proc.
559 Lunar Sci. Conf. 7, 2983–3005.
560 Sugita, S., Honda, R., Morota, T., Kameda, S., Sawada, H., Tatsumi, E., et al., 2019. The
561 geomorphology, color, and thermal properties of Ryugu: implications for parent-body
562 processes. Science 364, eaaw0422.
563 Tsujido, S., Arakawa, M., Suzuki, A.I., Yasui, M., 2015. Ejecta velocity distribution of impact
564 craters formed on quartz sand: effect of projectile density on crater scaling law. Icarus 262,
565 79–92.
566 Yamamoto, S., Wada, K., Okabe, N., Matsui, T., 2006. Transient crater growth in granular targets:
567 An experimental study of low velocity impacts into glass sphere targets. Icarus 183, 215-224.
568 Yasui, M., Arakawa, M., Okawa, H., Hasegawa, S., 2021. Impact cratering experiments on granular
569 targets simulating surface layer on asteroid 162173 Ryugu: Crater scaling law and impact
570 induced seismic shaking. Proc. 52nd Lunar and Planetary Science Conf., #1158.
571 Watanabe, S., Hirabayashi, M., Hirata, N., Hirata, N., Noguchi, R., Shimaki, Y., et al., 2019.
572 Hayabusa2 arrives at the carbonaceous asteroid 162173 Ryugu—A spinning top–shaped
573 rubble pile. Science 364, 268-272.

574

575 **Figure captions**

576

577 **Figure 1.** Schematic illustration of the ejection process during crater formation. The parameters

578 related to the π-scaling theory are introduced.

579

580 **Figure 2.** Image of the target used in run number 210318-1. Fifty-two tracer beads 3 mm in

581 diameter were placed on the target surface. High-speed cameras were taken from the upper side of

582 this image.

583

584 **Figure 3.** Snapshots from high-speed cameras taken from **(a)** the front and **(b)** the top at 2 ms after

585 the shot. Trajectories of tracer beads are shown by circles with the same colors (run number:

586 201002-6). **(c)** The 3D trajectories of the tracer beads shown in **(a)** and **(b)**. The tracer beads are

587 identified by numbers from 1 to 6.

588

589 **Figure 4.** Schematic illustration of the ejection vector of a tracer bead. The parameters analyzed in

590 this study are introduced. The x axis is defined as the line connecting the impact point with the

591 initial position of the tracer bead. The y axis is perpendicular to the x axis on the target surface.

592 The z axis is perpendicular to the xy plane.

593

594 **Figure 5.** A series of high-speed images of the crater formation process for run number 210317-8.

595 The label in the upper left corner of each image indicates the time passed after the impact.

596

597 **Figure 6. (a)** Ejecta velocity distribution described by the relationship between the initial position

598 normalized by the crater radius, r_0/R, and the ejection velocity, v_0, normalized by $\sqrt{gR}$, for the

599 low-velocity impact experiments. The solid lines show the results calculated from Eq. (13) for

600 a/R=0.04, 0.15 and 0.3. **(b)** Ejecta velocity distribution described by the relationship between $(r_0 -$

601 $a)/R$, and $v_0/\sqrt{gR}$. **(c)** Ejecta velocity distribution described by the relationship between $(r_0 +$

602 $a)/R$, and $v_0/\sqrt{gR}$. The solid line shows the result fitted by Eq. (13). **(d)** Ejecta velocity

603 distribution scaled by r_0/R in the horizontal axis for the high-velocity impact experiments. The

604 solid lines show the results calculated from Eq. (13) for a/R=0.04 and 0.15. **(e)** Ejecta velocity

605 distribution scaled by $(r_0 - a)/R$ in the horizontal axis for the high-velocity impact experiments.

606 **(f)** Ejecta velocity distribution scaled by $(r_0 + a)/R$ in the horizontal axis for the high-velocity

607 impact experiments. The symbol color shows the tracer bead radius normalized by the crater radius,

608 a/R, in all six panels.

609

610 **Figure 7.** Ejection velocity distributions of tracer beads. Blue and red symbols indicate the results

611 for low-velocity and high-velocity impact experiments, respectively. The symbol size corresponds

612 to the relative size of the tracer beads. The solid lines show the results fitted by Eq. (13).

613

614 **Figure 8. (a)** A snapshot of the ejecta curtain for run number 210318-1 taken by a high-speed
615 camera at 10 ms after the impact. The dotted rectangular area is enlarged and shown at the right
616 side; a tracer bead is seen at the bottom of the hole on the ejecta curtain. **(b)** Schematic illustrations
617 of the ejecta curtain growing with the tracer brads shown by the cross section and the front view.
618 On the illustration of the cross section, a tracer bead is shown at the initial position and at three
619 different positions (A, B, C) corresponding to each ejection velocity depending on the distance
620 from the impact point (r_0-a, r_0, r_0+a). The forbidden zone is colored grey, where a tracer bead
621 stopped the flow of fine glass beads, and the number density of fine glass beads are much smaller
622 than that of the surrounding density. The illustration of the front view can be compared with Fig.
623 8a to confirm the tracer bead position: The position C is achieved.

624

625 **Figure 9. (a)** Ejection angles of tracer beads described by the relationship between the initial
626 position normalized by the crater radius, r_0/R, and the ejection angle, θ. **(b)** Ejection angles of
627 tracer beads described by the relationship between $(r_0 + a)/R$, and θ. The solid lines show the
628 results fitted by Eq. (14). The symbol color and relative size show the tracer bead radius normalized
629 by the crater radius, a/R, in two figures.

630

631 **Figure 10.** Azimuthal angles of tracer beads described by the relationship between the initial
632 position normalized by the crater radius, r_0/R, and the azimuthal angle, ϕ. The symbol color and
633 relative size show the tracer bead radius normalized by the crater radius, a/R.
634
635 **Figure 11. (a)** Successive images of ejection of a tracer bead taken by the high-speed camera shown
636 at every 30 ms. The rotation of the tracer bead was observed together with the ejecta curtain growth.
637 **(b)** Selected enlarged images of the tracer bead in Fig. 11a. WS labelled on the bead is a white
638 stripe painted on the bead to recognize the rotation, and it enabled us to determine the rotation
639 direction and the rotation speed of the bead.
640
641 **Figure 12.** Ejection velocity distributions of tracer beads with different buried depth. The dotted
642 line is fitted by a least square method for the data of tracer beads put on the surface. The solid line
643 is calculated by Eq. (13). The closed symbol was derived from the tracer bead buried completely.
644
645 **Figure 13. (a)** Ejection velocity distributions of tracer beads obtained for the low- and high-
646 velocity impact experiments. The solid curves show the results fitted by Eq. (16). **(b)** Ejection angle
647 distribution of tracer beads. The solid curve shows the result fitted by Eq. (17). The symbol color
648 and relative size show the tracer bead radius normalized by the crater radius, a/R, in two figures.
649

Figure 14. Schematic illustration showing the ejection and the rotation mechanism of the tracer bead.

Figure 15. Contour plot of the normalized landing point, L/R, changing with the normalized boulder radius, a/R, and the normalized initial position, r_0/R. The color shows the value of L/R. The ranges of $a/R > r_0/R$ and $a/R > -r_0/R + 1.23$ are not drawn.

Figure 16. Ejecta velocity distributions for boulders with sizes of $a/R = 0.04–0.40$. The dotted line represents the normalized ejection velocity for the SCI crater. The dash-dotted line represents the normalized ejection velocity for the Urashima crater.

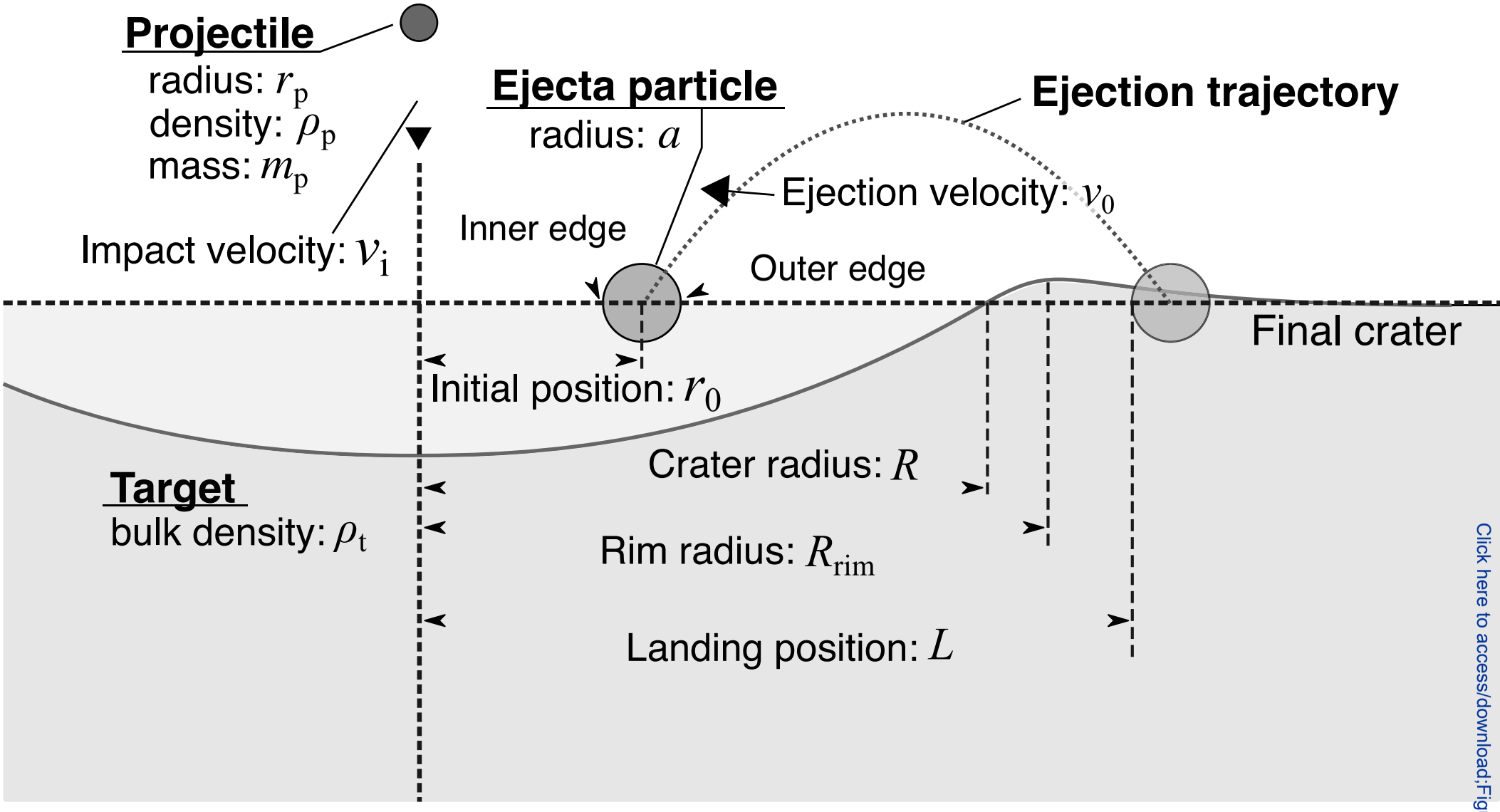

Figure2

Click here to access/download;Figure;Fig2.eps

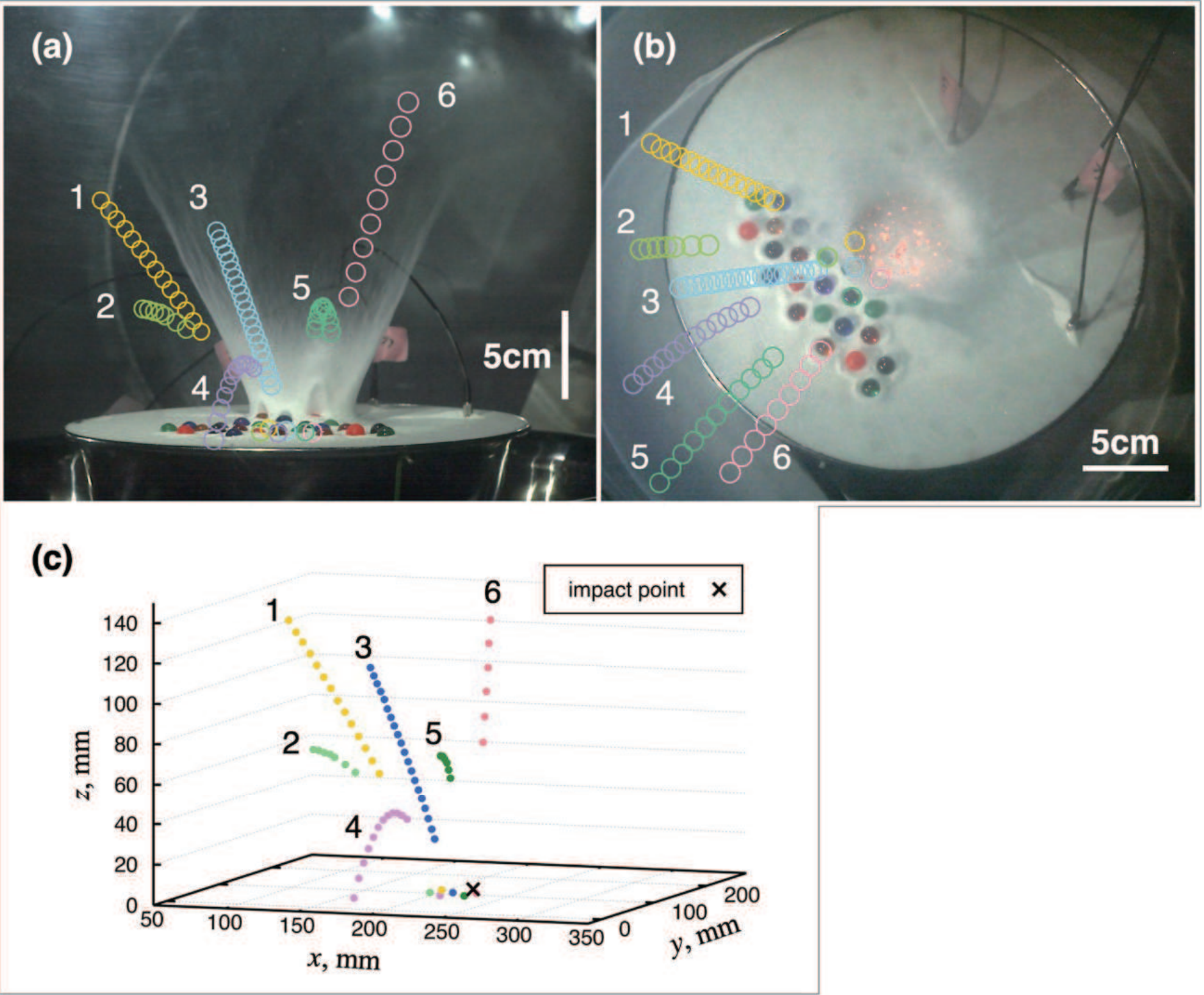

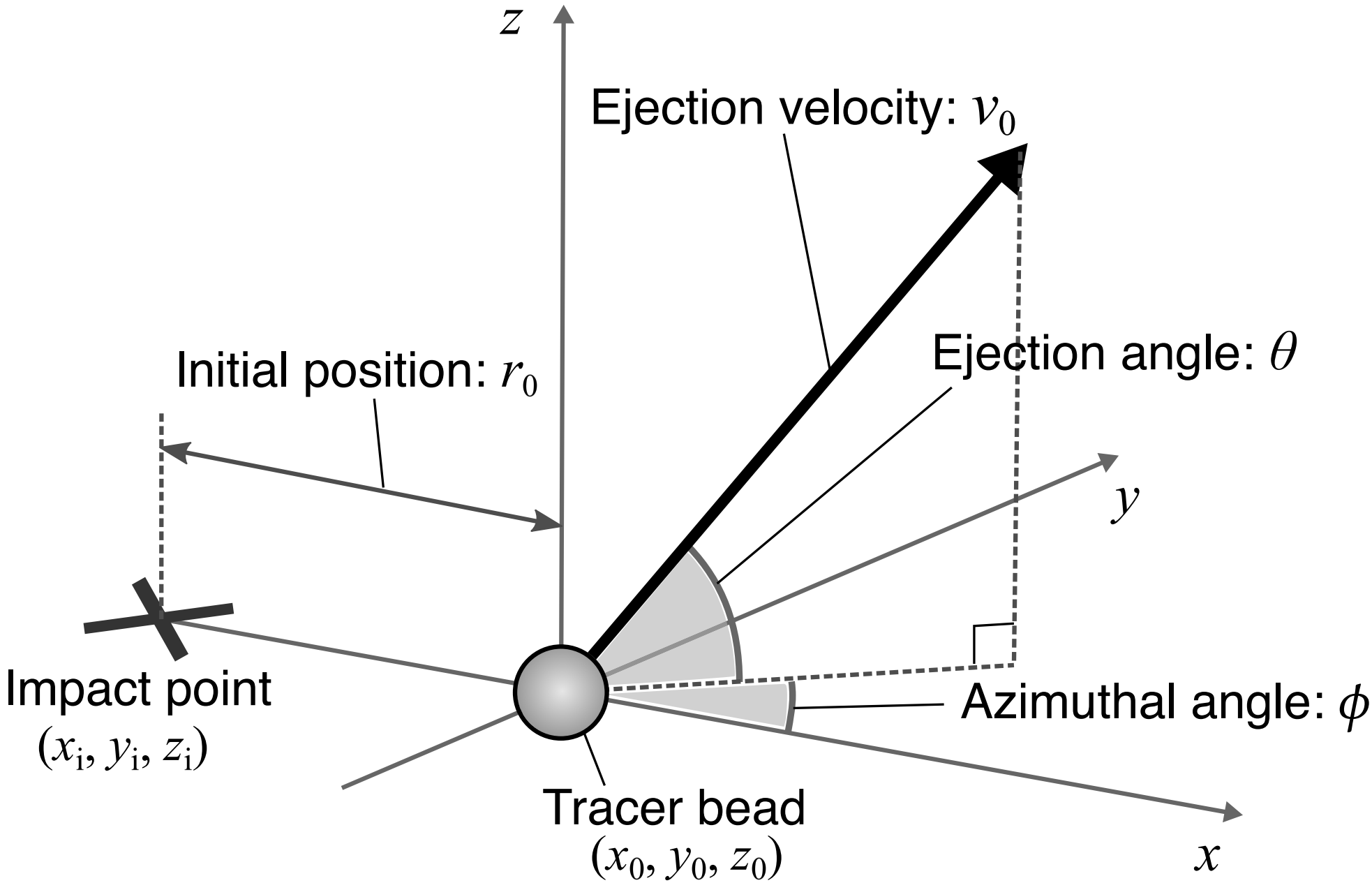

Figure5

Click here to access/download;Figure;Fig5.tiff

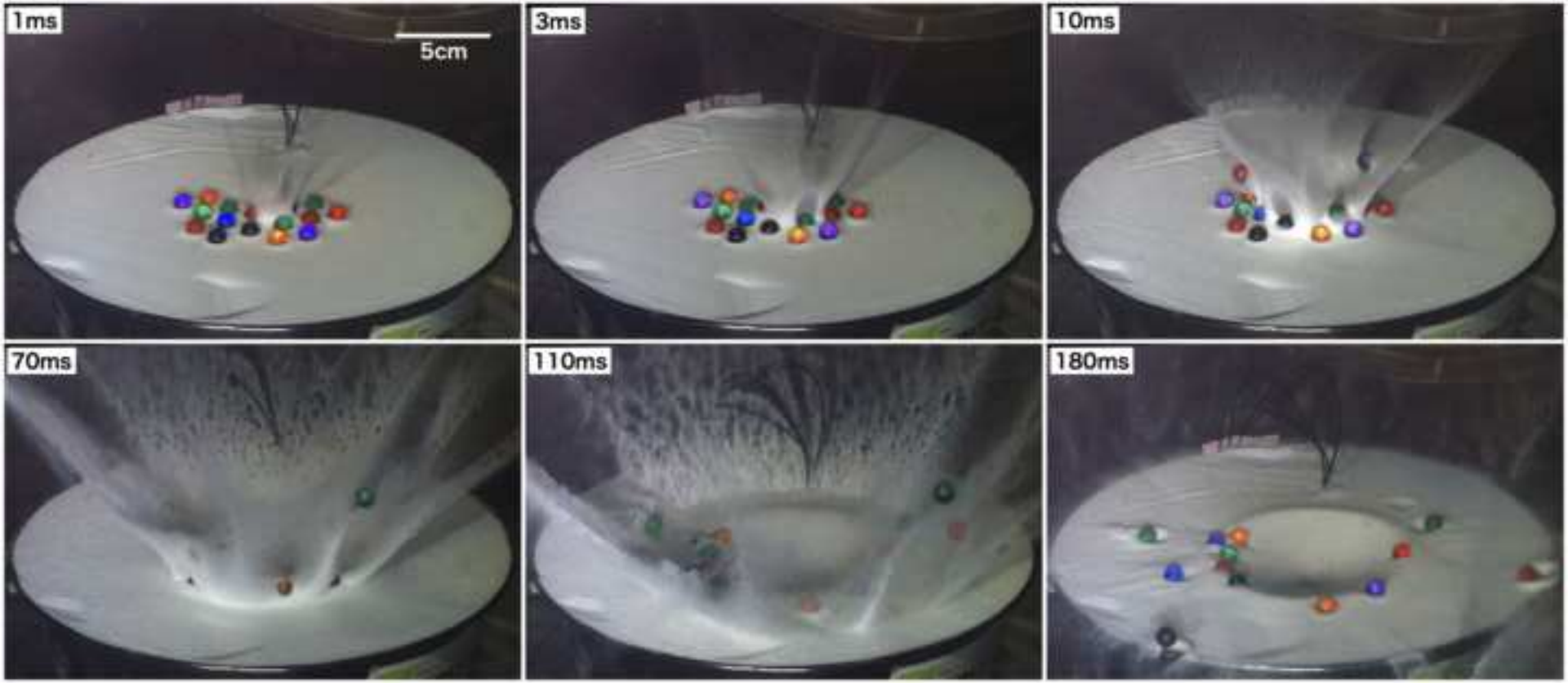

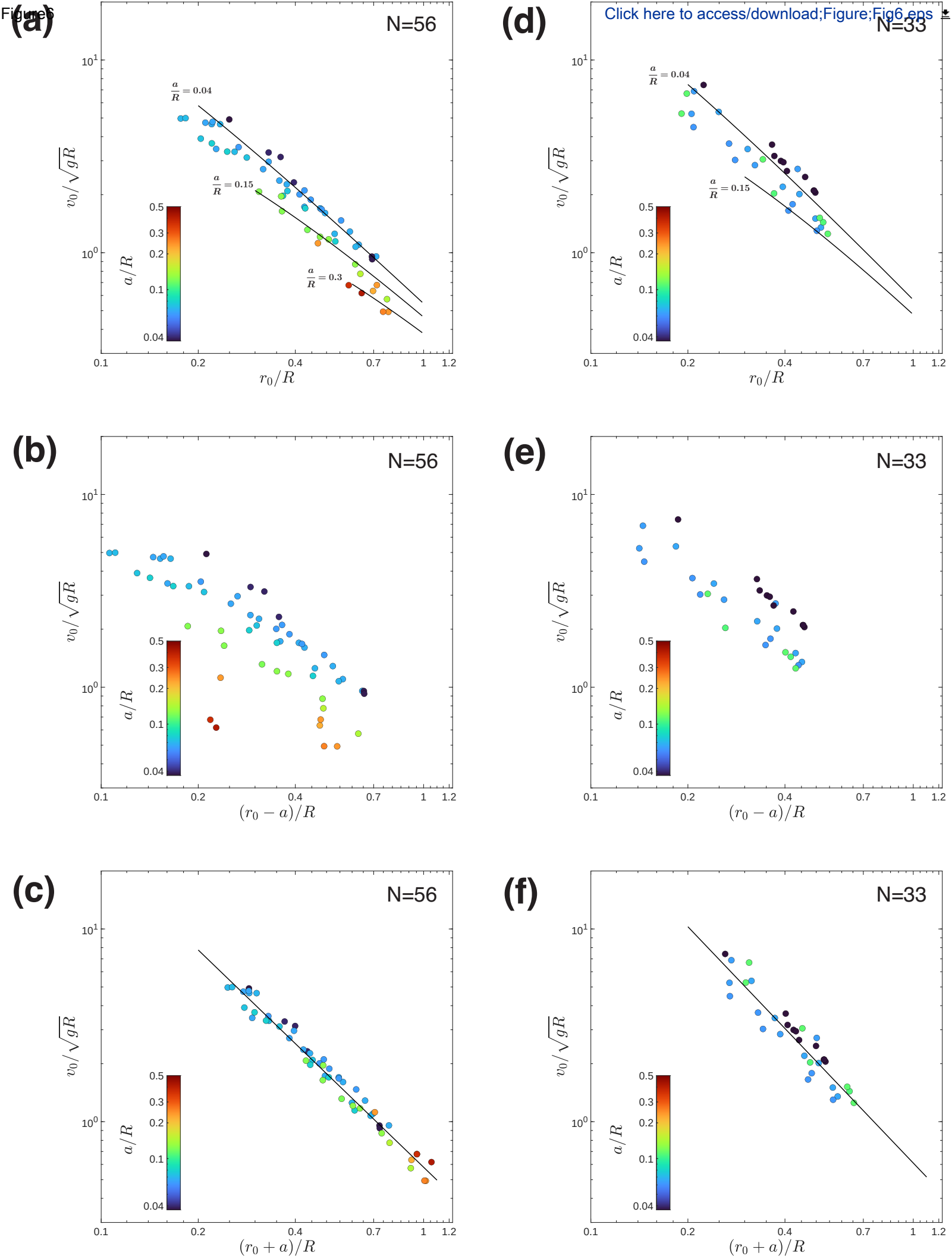

Figure7

Click here to access/download;Figure;Fig7.eps

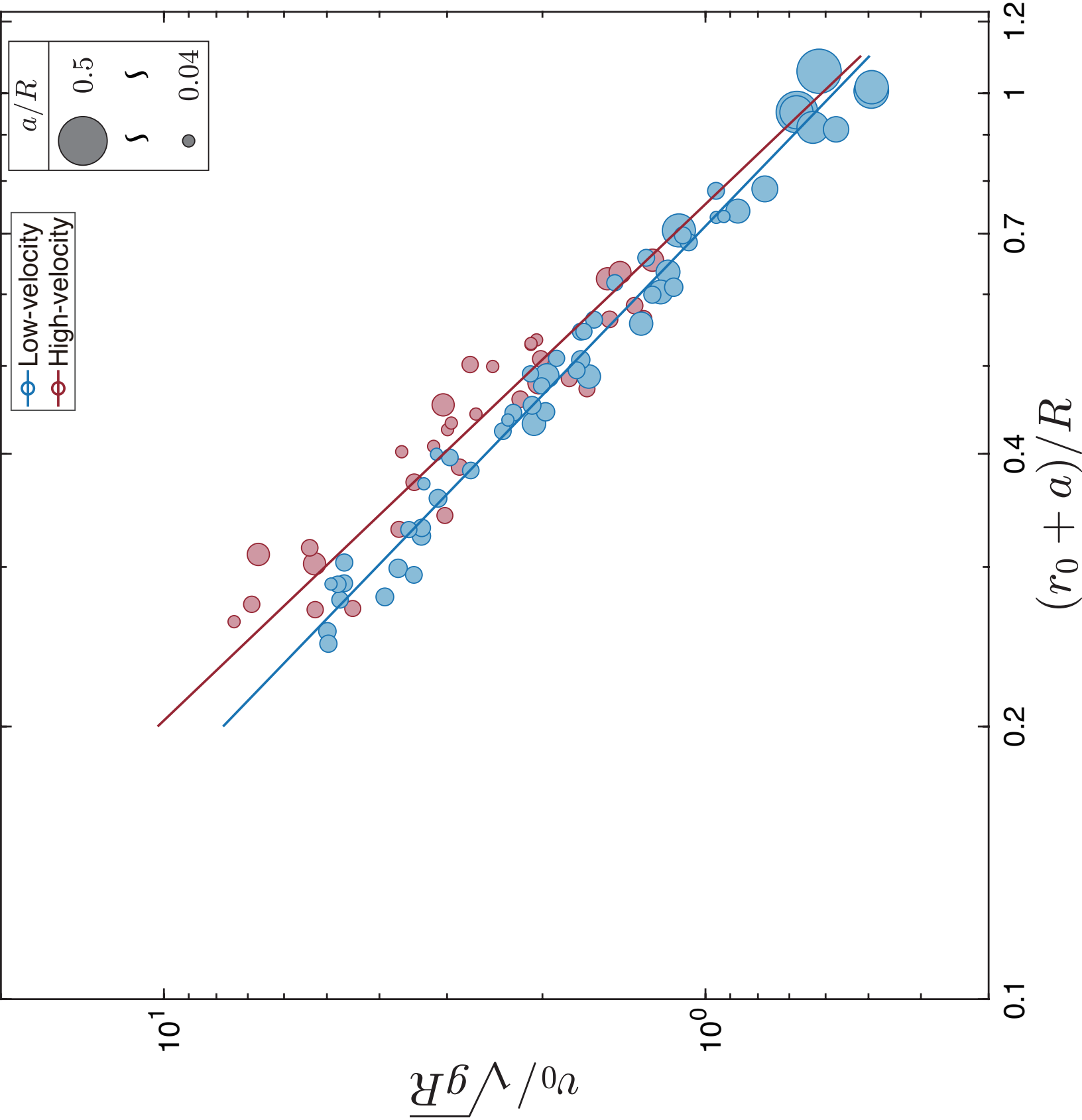

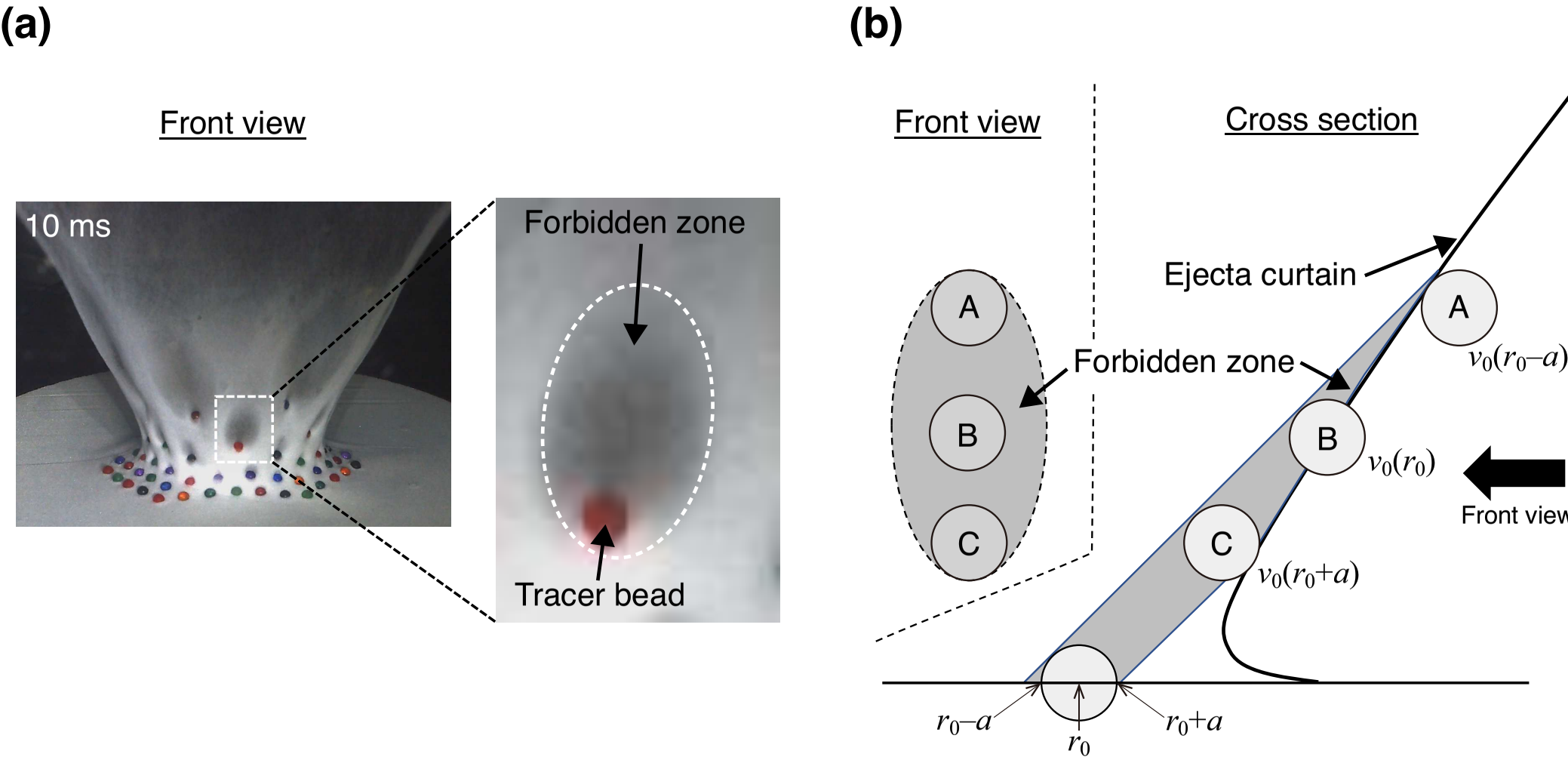

Figure9

Click here to access/download;Figure;Fig9.eps

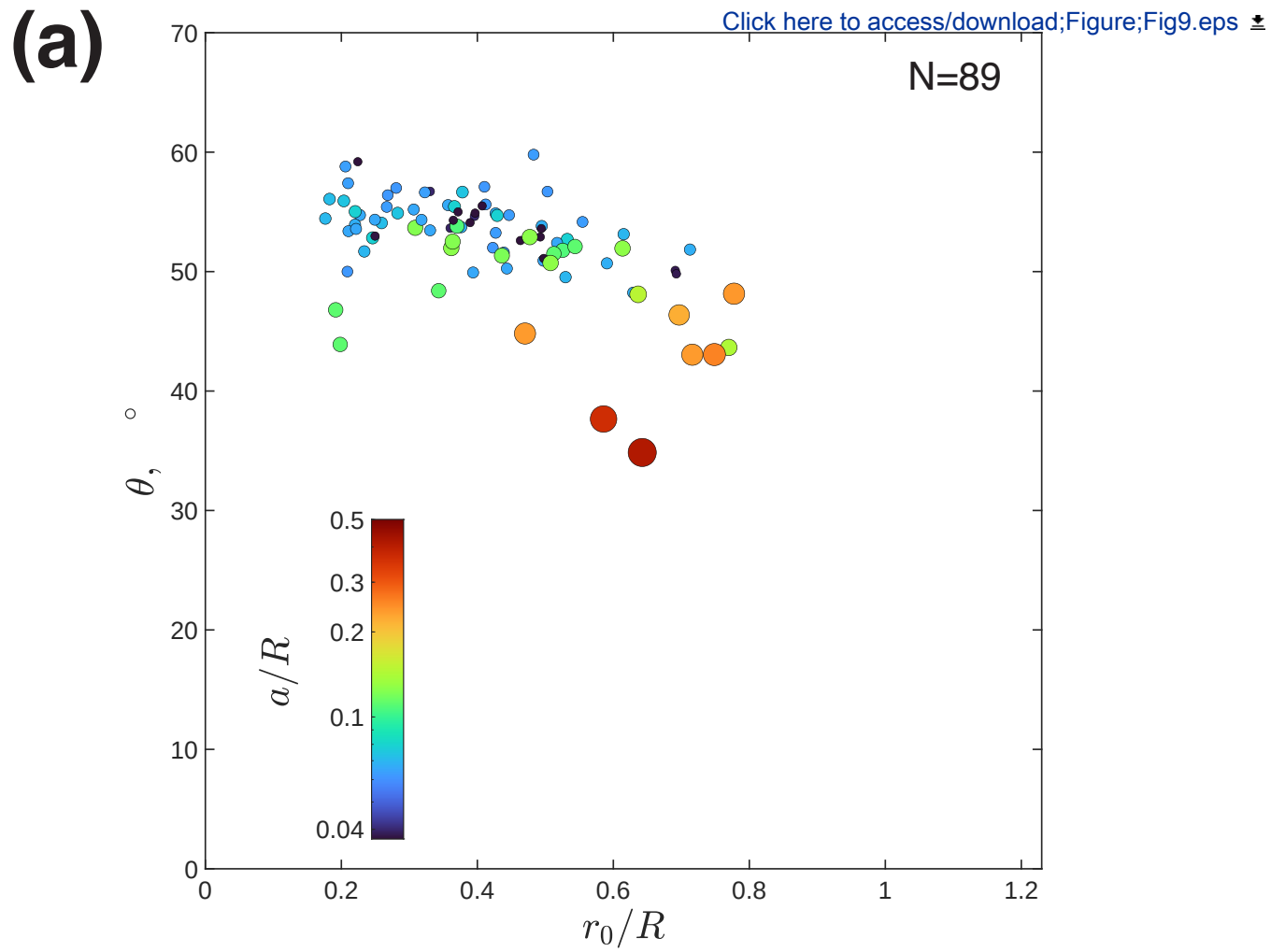

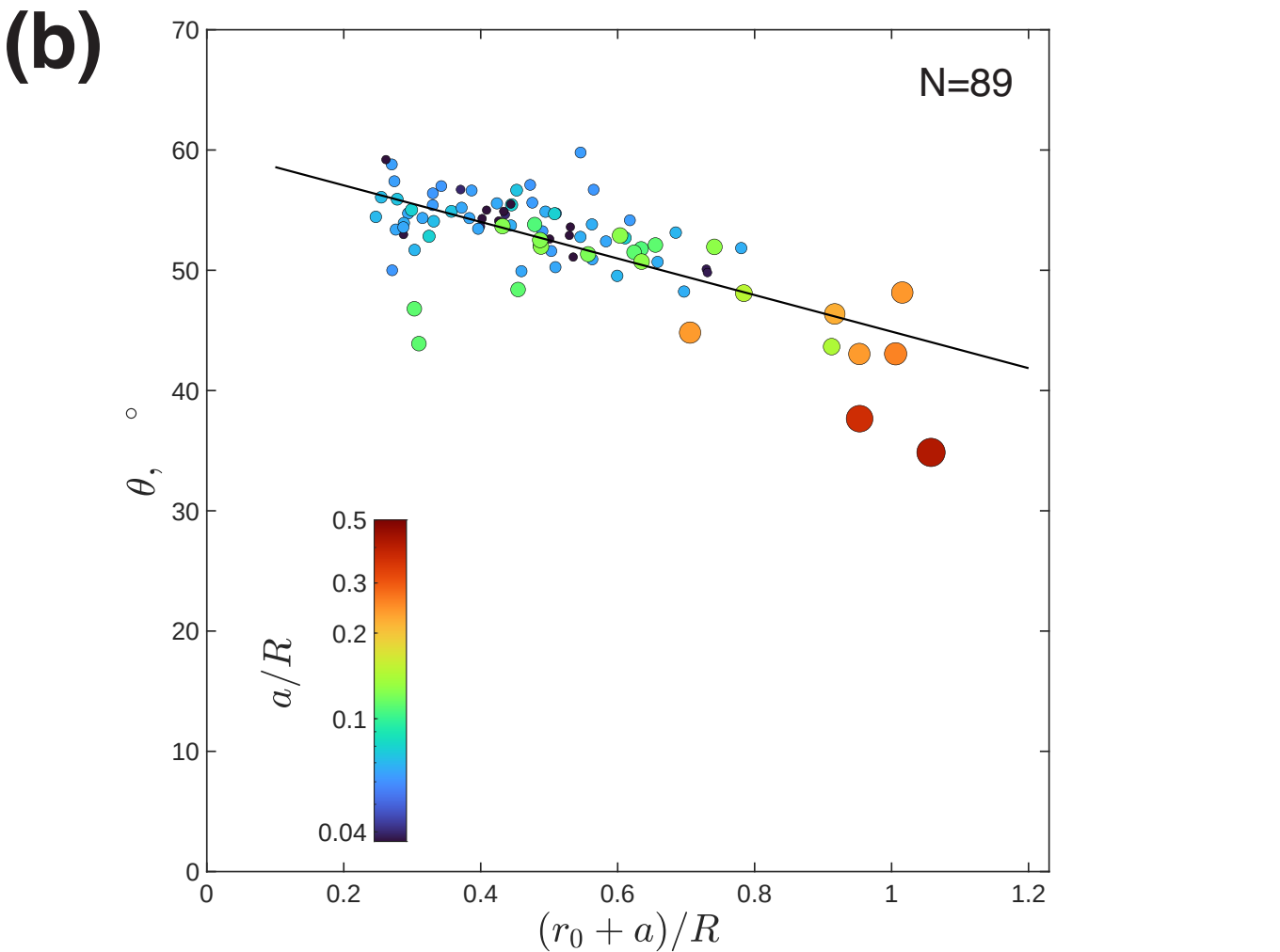

Figure10

Click here to access/download;Figure;Fig10.eps

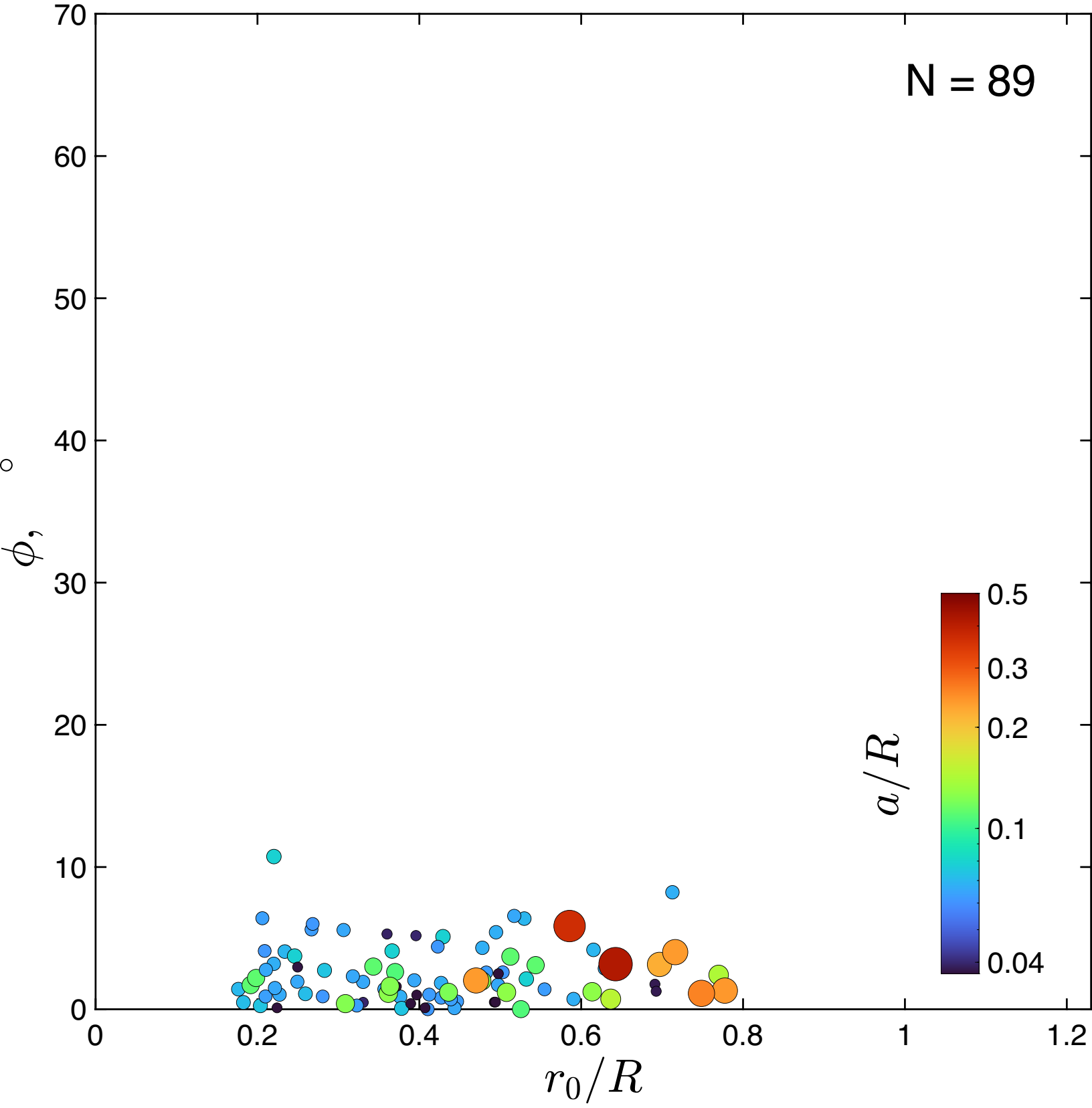

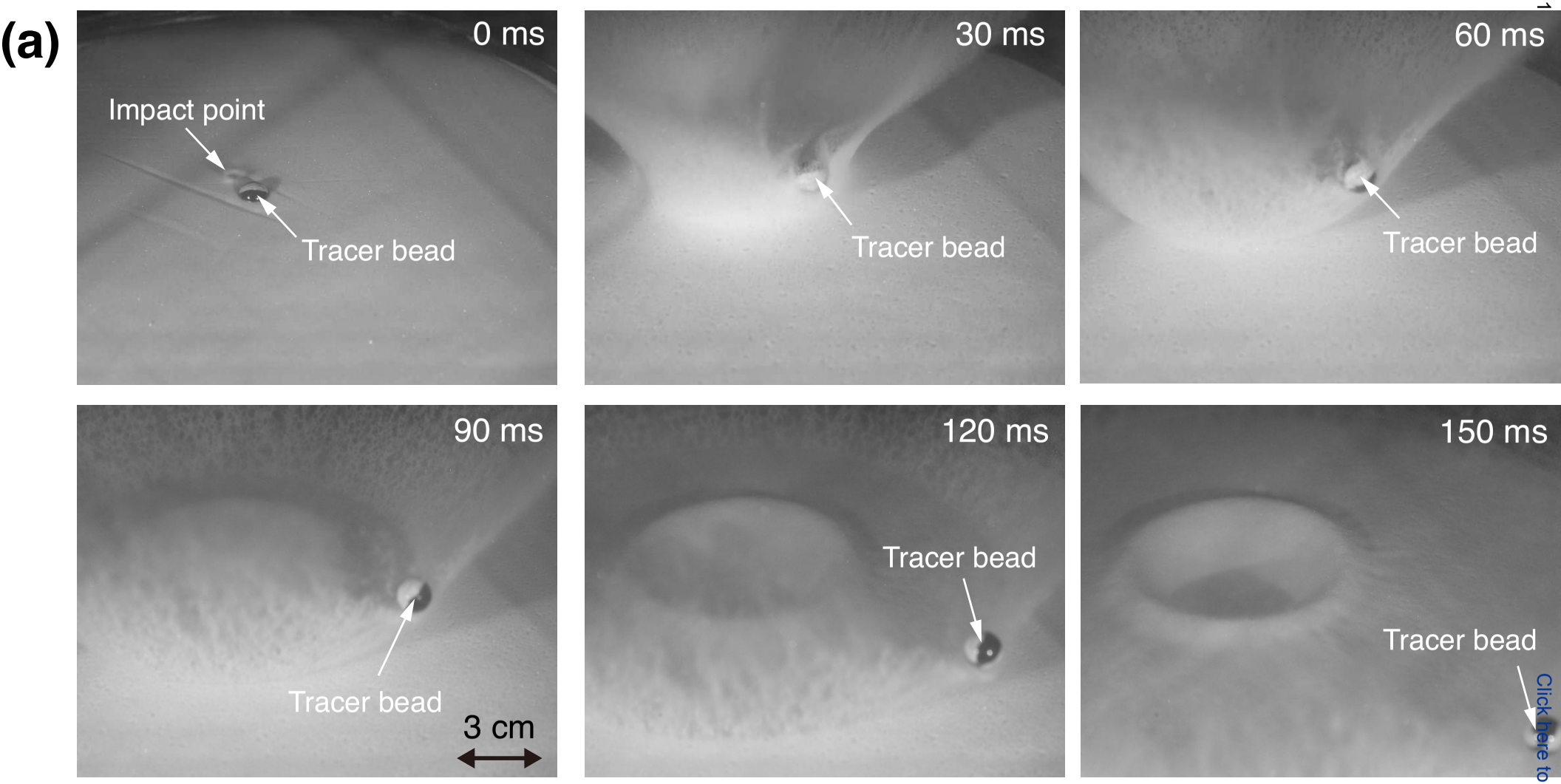

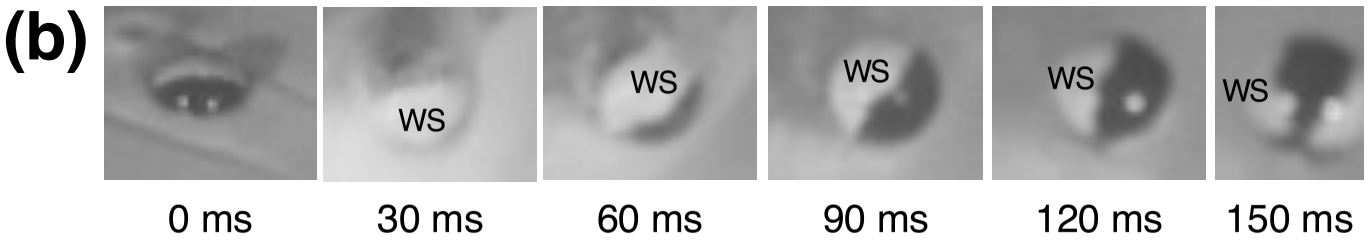

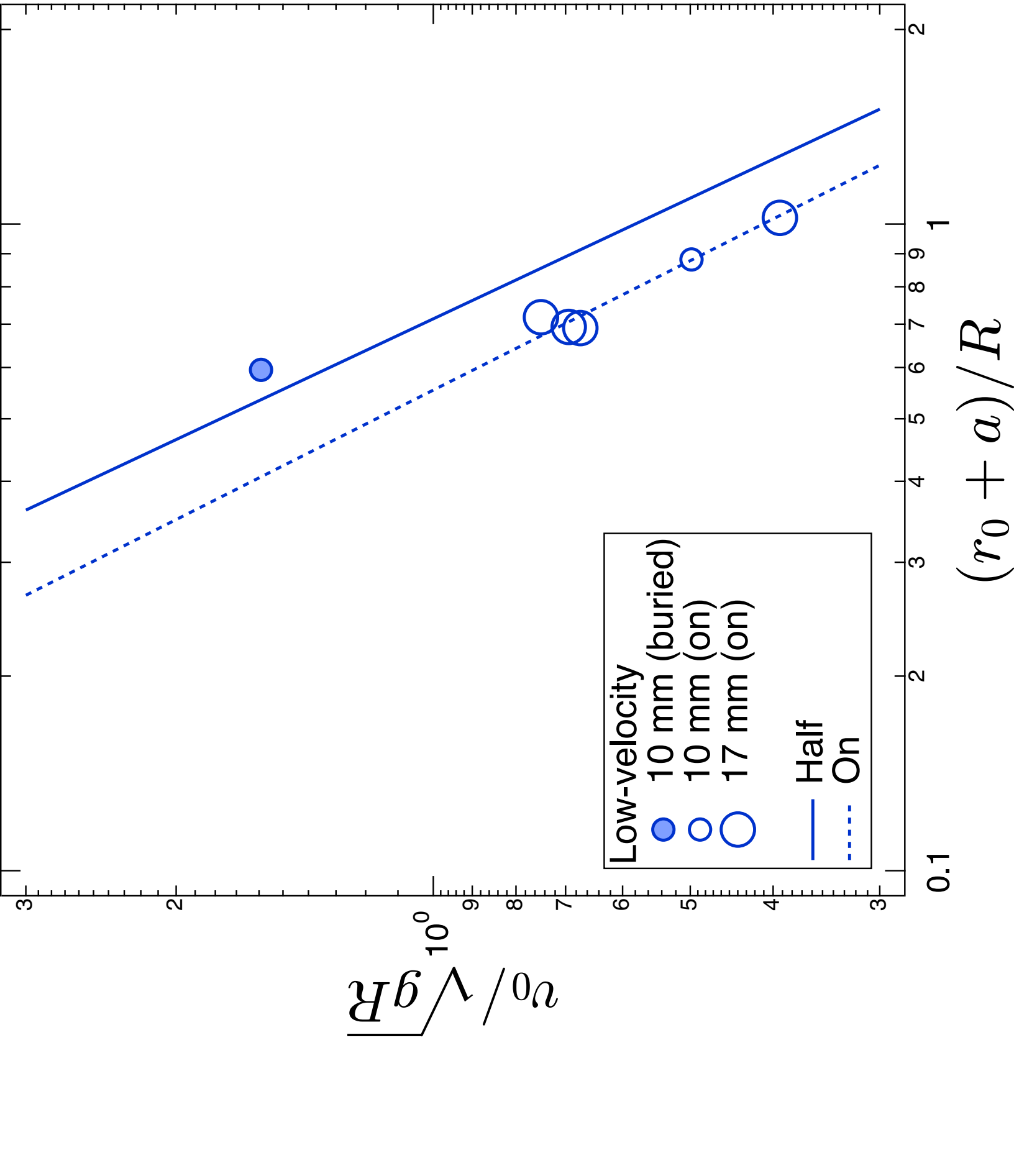

Figure13

Click here to access/download;Figure;Fig13.eps

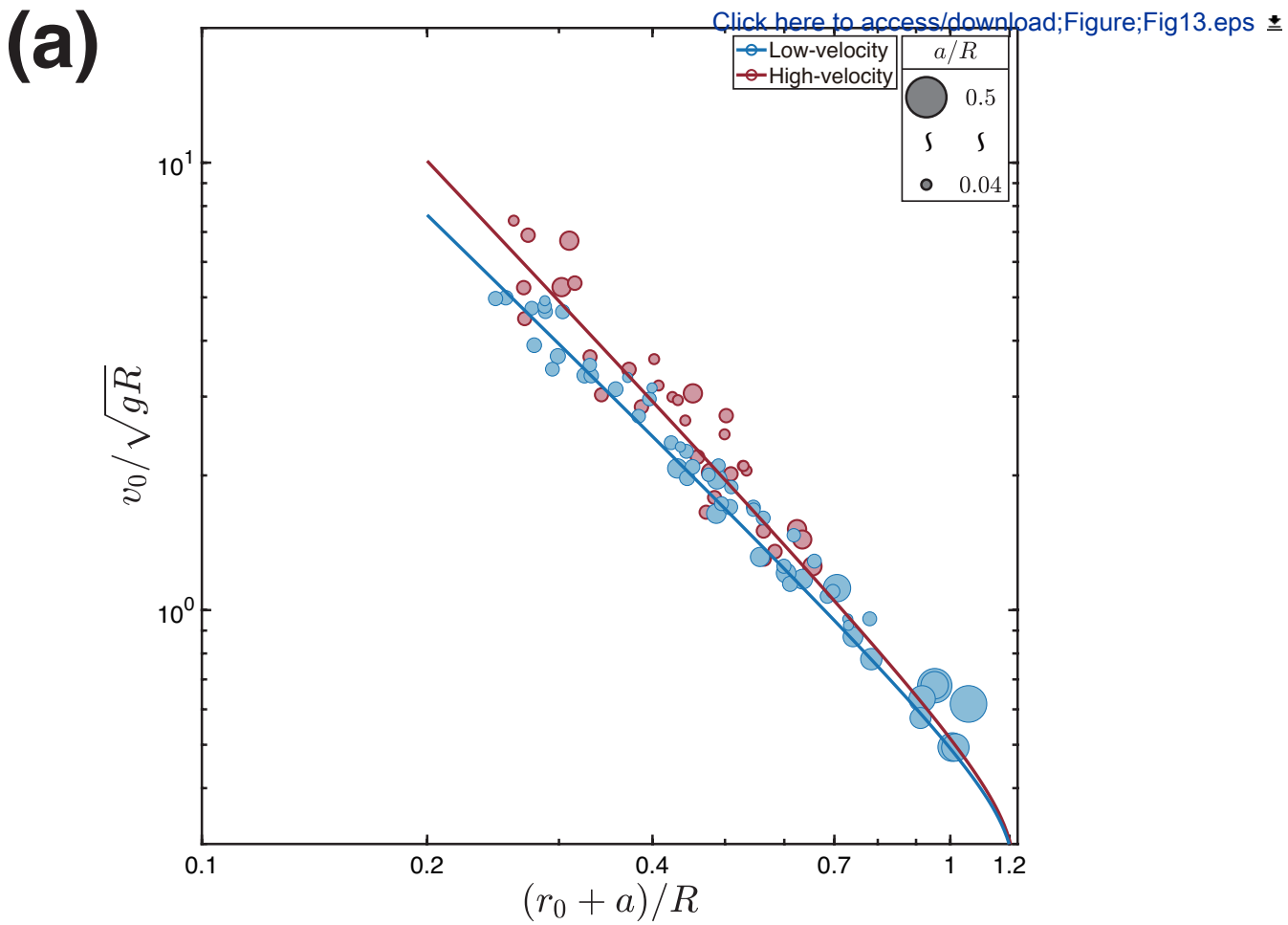

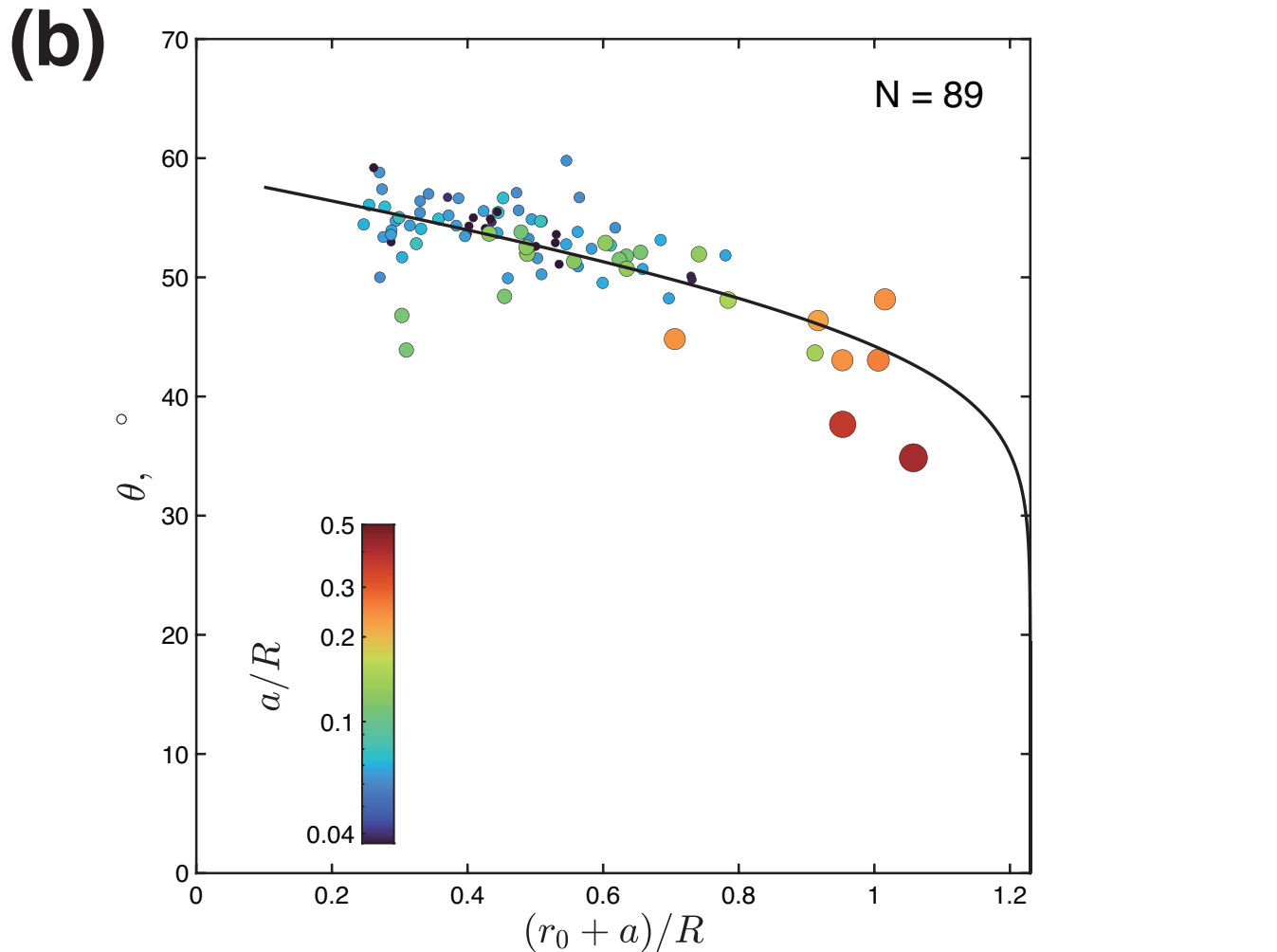

Figure14

Figure15

Click here to access/download;Figure;Fig15.eps

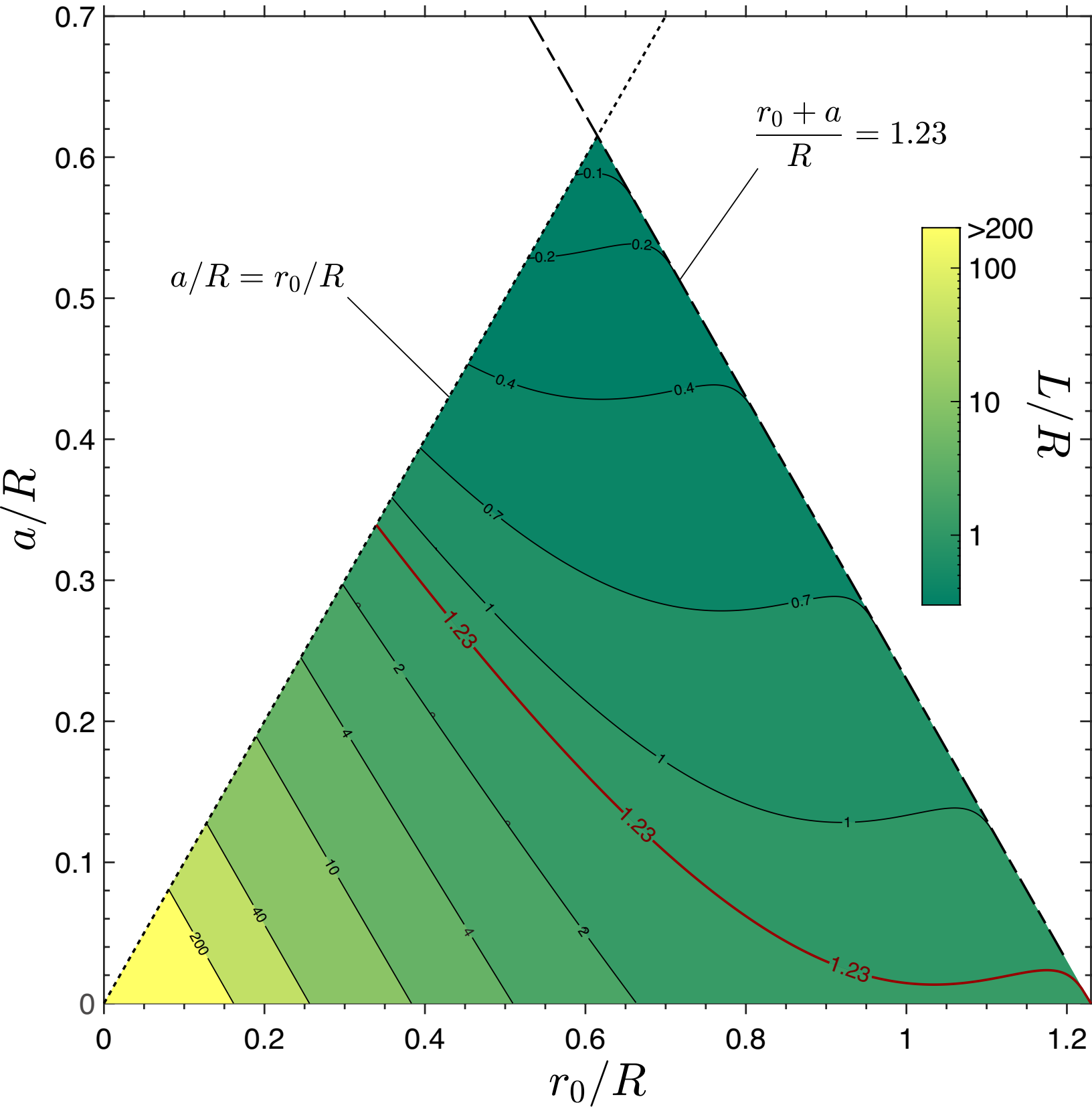

Figure16

Click here to access/download;Figure;Fig16.eps

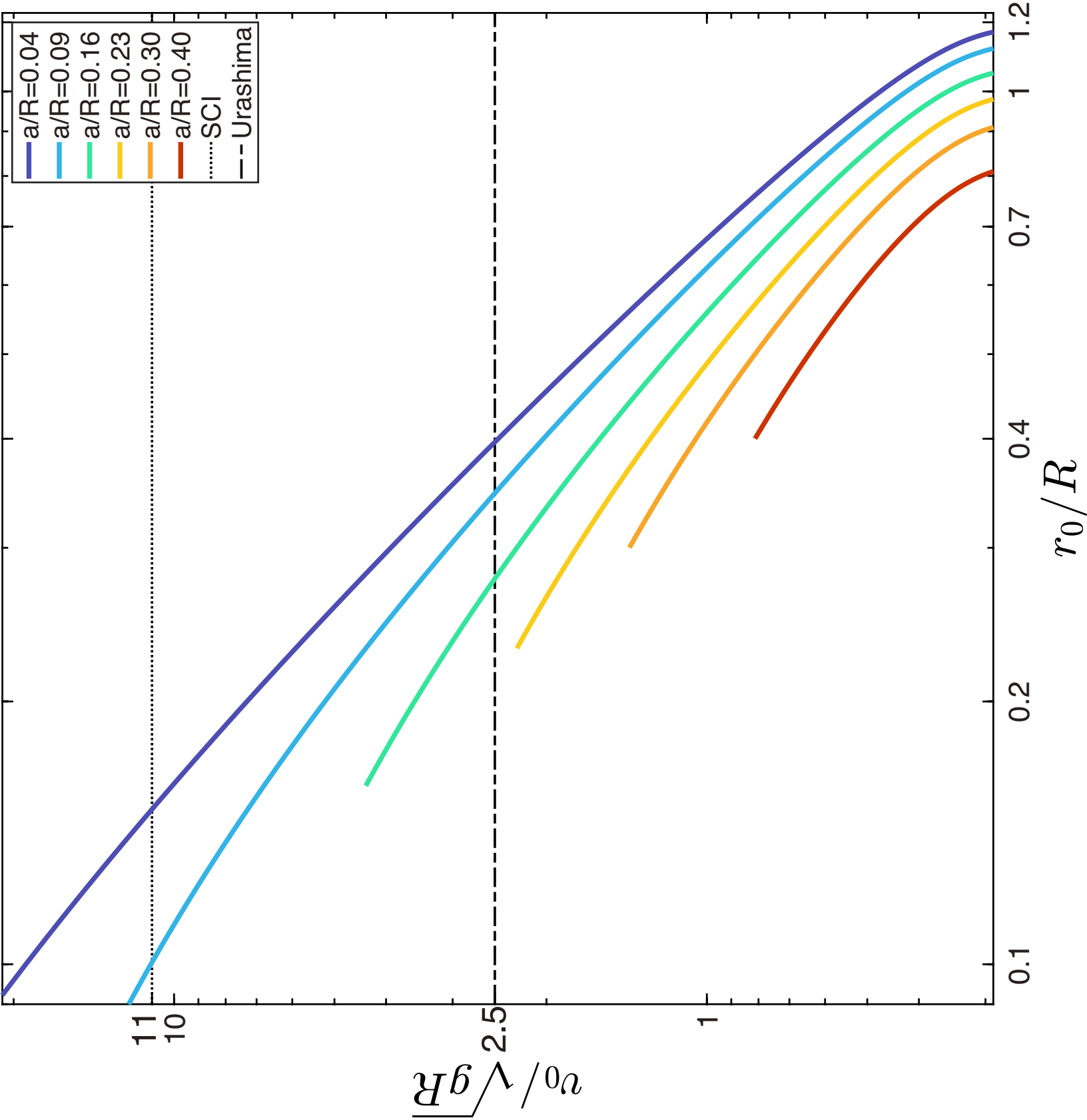

Table 1. Experimental conditions and results according to crater rim radius

Run number	Projectile diameter $2r_p$ [mm]	Projectile mass m_p [mg]	Impact velocity v_i [m s^{-1}]	Crater rim radius R_{rim} [mm]	Diameter of tracer beads [mm]
200309-3	3.0	112	144.1	46.0	3, 5
200309-4	3.0	112	133.3	43.6	3, 5
200309-5	3.0	112	165.6	46.0	3, 5
200309-6	3.0	112	175.4	46.7	3, 5
200310-1	3.0	112	161.3	45.4	5
200310-2	3.0	112	138.9	42.6	5
200310-3	3.0	112	115.7	41.3	5
200312-1	3.0	112	161.3	45.4	5
200312-2	3.0	112	125.3	44.1	5
200312-3	3.0	112	188.0	48.7	5
200312-5	3.0	112	104.6	39.1	5
200930-2	1.0	4.2	2129	46.8	5
201001-1	1.0	4.0	4417	56.5	10
201001-2	2.0	33.5	4132	96.1	10
201002-6	2.0	33.5	4098	99.5	10
201117-3	2.9	112	178.6	49.7	10
201126-1	3.0	112	190.8	50.0	10
201126-2	3.0	111	171.8	44.6	10
201126-3	2.9	111	140.1	43.1	10
201130-1	3.0	113	162.3	47.4	17
201130-2	3.0	113	147.5	44.0	17

201201-10	3.0	112	133.0	85.3	10
201204-1	3.0	112	101.2	40.6	17
201204-2	3.0	113	115.9	44.2	17
201207-1	3.0	112	181.2	49.9	30
201207-2	2.9	111	154.8	43.9	30
210106-1	3.0	113	146.2	44.5	17
210106-6	2.9	111	165.6	94.3	17
210112-1	3.0	113	180.5	100.0	17
210112-2	3.0	113	184.5	98.9	17
210112-6	3.0	112	108.7	79.9	17
210118-6	3.0	113	147.1	94.3	10
210317-8	1.0	3.9	4419	55.2	10
210318-1	2.0	33.3	1925	82.3	5
210318-4	2.0	33.4	1943	83.4	5
210716-1	3.0	113	163.9	48.9	3
210716-2	3.0	113	181.2	48.6	10
210718-1	3.0	112	174.8	50.9	10
210718-2	3.0	112	174.2	49.9	10
210718-3	3.0	112	156.7	46.9	5
210718-4	3.0	112	154.3	48.0	3

Table 2. Experimental results for ejected tracer beads

Run number	Bead ID	Bead Diameter [mm]	Initial position [mm]	Ejection velocity [m s^{-1}]	Ejection angle θ [°]	Azimuthal angle [°]
Low-velocity experiments						
200309-3	1	5	8.5	2.1	54.7	1.0
	2	3	14.8	1.4	54.6	5.2
200309-4	1	5	6.3	2.9	54.4	1.4
200309-5	1	3	12.4	2.0	56.7	0.5
	2	5	13.4	1.4	55.6	1.4
200309-6	1	3	13.7	1.9	53.6	5.3
	2	5	12.6	1.8	53.5	1.9
200310-1	1	5	13.9	1.4	53.7	0.9
	2	5	17.6	1.0	52.8	4.3
	3	5	8.1	2.8	53.9	3.2
200310-2	1	5	6.3	2.9	56.1	0.5
	2	5	9.0	1.9	54.1	1.1
200310-3	1	5	6.8	2.2	55.9	0.3
	2	5	9.5	1.8	54.9	2.7
	3	5	12.7	1.2	56.7	0.1
200312-1	1	5	18.3	1.0	53.8	5.4
	2	5	26.3	0.6	51.8	8.2
	3	5	15.8	1.0	54.9	1.8
	4	5	21.8	0.8	50.7	0.7
	5	5	23.2	0.7	48.2	2.9
200312-2	1	5	22.1	0.6	53.1	4.2
	2	5	19.0	0.7	49.5	6.4
	3	5	8.4	2.8	51.7	4.1
200312-3	1	5	10.6	2.2	55.4	5.6
	2	5	16.9	1.3	53.2	0.8
	3	5	19.1	1.0	59.8	2.6
	4	5	16.3	1.3	55.6	1.0
	5	5	22.0	0.9	54.2	1.4
	6	5	17.7	1.2	54.7	0.5
200312-5	1	5	7.0	2.1	55.0	10.7
	2	5	11.6	1.1	55.4	4.1
	3	5	7.8	1.9	52.8	3.7

	4	5	16.9	0.6	52.7	2.1
	5	5	13.6	0.9	54.7	5.1
201117-3	1	10	24.8	0.5	51.9	1.2
201126-1	1	10	20.7	0.7	50.7	1.2
201126-2	1	10	28.0	0.4	43.6	2.4
201126-3	1	10	22.3	0.5	48.1	0.7
201130-1	1	17	26.9	0.4	46.4	3.2
201130-2	1	17	27.8	0.3	48.1	1.3
201204-1	1	17	24.7	0.3	43.1	1.1
201204-2	1	17	25.8	0.4	43.0	4.0
210106-1	1	17	17.0	0.7	44.8	2.0
201207-1	1	30	23.8	0.4	37.7	5.9
201207-2	1	30	23.0	0.4	34.9	3.2
210716-1	1	3	9.9	3.1	53.0	3.0
210716-2	1	10	18.9	0.8	52.9	2.0
	2	10	14.3	1.2	52.0	1.1
210718-1	1	10	18.1	0.8	51.3	1.2
210718-2	1	10	14.8	1.0	52.5	1.6
	2	10	12.5	1.3	53.7	0.4
210718-3	1	5	8.0	2.9	53.4	2.8
	2	5	8.5	2.9	53.6	1.5
	3	5	12.1	1.7	54.3	2.3
210718-4	1	3	27.0	0.6	50.1	1.8
	2	3	27.0	0.6	49.8	1.3
201201-10*	1	10	23.8	0.3	41.7	–
210106-6*	1	17	17.6	0.4	55.4	–
210112-1*	1	17	18.1	0.4	52.8	–
210112-2*	1	17	17.8	0.4	54.2	–
210112-6*	1	17	22.9	0.2	45.6	–
210118-6**	1	10	16.4	0.9	38.0	–
High-velocity experiments						
200930-2	1	5	9.5	3.3	54.3	1.9
	2	5	11.7	2.1	55.2	5.6
	3	5	15.0	1.3	49.9	2.0
	4	5	16.9	1.2	50.3	0.1
	5	5	18.9	0.9	50.9	1.7
	6	5	19.7	0.8	52.4	6.6

201001-1	1	10	24.2	1.0	51.8	0.0
	2	10	17.0	1.4	53.8	2.6
201001-2	1	10	25.3	2.5	56.6	0.3
	2	10	16.4	6.0	57.4	0.9
	3	10	16.1	4.6	58.8	6.4
	4	10	34.3	2.4	51.6	0.7
201002-6	1	10	22.7	2.7	57.0	0.9
	2	10	16.9	4.0	50.0	4.1
	3	10	21.7	3.3	56.4	6.0
	4	10	33.2	1.5	57.1	0.0
	5	10	40.7	1.2	56.7	2.6
	6	10	34.2	1.6	52.0	4.4
210317-8	1	10	8.6	3.5	46.8	1.7
	2	10	15.4	2.0	48.4	3.0
	3	10	23.0	1.0	51.5	3.7
	5	10	8.9	4.4	43.9	2.2
	6	10	24.4	0.8	52.1	3.1
210318-1	1	5	15.0	6.0	59.2	0.1
	2	5	24.4	2.9	54.3	1.1
	3	5	31.0	2.0	52.6	2.3
	3	5	33.3	1.7	51.1	2.5
210318-4	1	5	33.4	1.7	52.9	0.5
	2	5	26.4	2.4	54.1	0.4
	3	5	33.5	1.7	53.6	0.5
	4	5	27.6	2.2	55.5	0.1
	5	5	25.2	2.6	55.0	1.6
	6	5	26.9	2.4	54.9	1.0

* The tracer bead was put on the target surface.

** The tracer bead was completely buried in the target.